MASTER

Small particle expansion for electromagnetic detection (SPEED) applied to diffraction gratings

Sprée, M.

Award date:
2009

technische universiteit eindhoven
Faculty of Electrical Engineering
Division Electromagnetics and Wireless

Small Particle Expansion for Electromagnetic Detection (SPEED) applied to Diffraction Gratings

by M. Sprée

EMW-3-09

February, 2009

Graduation report performed at
TU/e, Electromagnetics and Wireless Section

Supervisors:
dr.ir. T.E. Motoasca
prof. dr. A.G. Tijhuis

Contents

Chapter 1

Introduction

1.1 Scope of thesis

The electromagnetic modeling of reflection and transmission gratings has attracted considerable theoretical and practical interest in the last decades.

In general, a diffraction grating can be defined as a periodic structure placed on the interface between two half spaces with different electromagnetic properties [1]. When the grating is illuminated by a monochromatic electromagnetic plane wave, a discrete number of reflected waves results. Only a small number of propagating reflected waves, or spectral orders, contribute to the scattered field far away from the diffraction grating. The direction of the reflected waves, corresponding to the spectral orders, depends on the angle of incidence and wavelength of the incident field and on the period of the structure. The propagated reflected waves can be used to obtain information about the geometry of the grating.

In novel lithography machinery periodic structures are placed on a wafer (a silicon substrate) for positioning purposes. From the diffracted waves, information about the shape of the structure and the position can be retrieved with an accuracy in the order of nanometers [2]. An example of a binary grating is shown in Fig. 1.1. To reconstruct the parameters of the actual geometrical dimensions of the grating, the scattered computed field is compared with the measured field. The actual geometrical parameters are retrieved by varying the parameters in the computed model and minimizing the difference with the measured data by using optimization techniques. For diffraction gratings applied in lithography machinery, the challenge is to compute rapidly and accurately the scattered electric field and the geometrical parameters of the structure.

To calculate the reflected field originated from a diffraction grating as an electromagnetic scattering problem, numerous computational solution techniques are developed such as the Rigorous-Coupled-Wave Approach (RCWA), differential equation methods and integral equation methods [2] [3].

In the present thesis we will focus on a domain integral equation method [4] [5]. The basic idea of this method is to represent the electromagnetic field scattered by an object in free space in terms of secondary sources or contrast currents inside the domain of the object. Via constitutive relations, the contrast currents are expressed in terms of the total field. Then, by the integration of

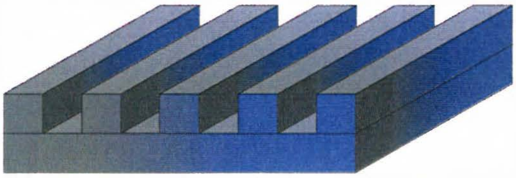

Figure 1.1: Example of a binary diffraction grating.

the contrast currents, an integral representation for the scattered electromagnetic field is obtained. The total field is defined as the sum of the scattered field and the incident field from which, by imposing the boundary conditions, an integral equation for the total field results. To find the total field, the object is discretized in a number of subdomains, where at each subdomain the total field is expanded into a (finite) set of basis functions. By substituting the expanded field in the integral equation and taking at both sides of the equation the inner product with the testing functions, the integral equation reduces to a system of linear equations. This system must be solved to find the weighting constants corresponding to the basis functions. The described method is known as the method of moments (MoM).

For periodic structures, the integral equation has as kernel a periodic Green's function which results in repeated evaluation of the domain integral. Without precautions, the evaluation of the Green's function series leads to large computation times as a consequence of the slow convergence of the series.

Several authors have proposed acceleration techniques to reduce the computation time for evaluating Green's function series. By applying a spectral and spatial decomposition of the kernel of the integral equation and simultaneously making use of Kummer's, Ewald's, Poisson's or Shank's transformations, the rate of convergence of the Green's function series improves considerably [6] [7]. In [7] a special combination of the first three mentioned transformation techniques has drastically enhanced the convergence and reduced the computation time to evaluate the integral equation with a periodic kernel. The general solution strategy for evaluating the integral equation is to decompose the periodic kernel in terms of a singular and a regular part. The domain integral, with singular kernel, can in general be written in a closed form, therefore solved analytically. For the domain integral with regular part, numerical quadrature schemes are required to accurately compute these integral contributions.

To find the electromagnetic field in the diffraction grating accurately, a large number of subdomains inside the object should be defined to approximate the electromagnetic field. By applying the method of moments a large system of equations results. Although the diffracted electromagnetic field will be found accurately, the numerical solution strategy leads to relative large computation times, but the parameters related to the shape of the periodic structure can be found accurately.

1.2 Objective and outline of the solution

The objective of this thesis is to develop a fast and efficient solving strategy for the electromagnetic scattering problem for a periodic object placed on the interface between two half spaces. The general idea to accomplish this is based on the assumption that the wavelength of the electromagnetic field inside the object is large compared to the dimensions of the object. Therefore, the electromagnetic field can be expanded in a combination of linear basis functions. For this case, the object is divided into a small number of subdomains. In the formulation of the scattering problem the evaluation of the domain integral is restricted to only one single period of the structure. Hence, the convergence problems disappear. By applying the point matching method, a special case of the method of moments with linear basis functions and Dirac delta functions as test functions, a relative small system of linear equations formulated in a closed form results. This approach is extremely suitable to rapidly retrieve information about the geometrical parameters of the diffraction grating with limited accuracy. These retrieved parameters can be used as a initial estimate in more accurate but slower solution techniques.

As a proof of principle, in this thesis, we only consider dielectric diffraction gratings which are periodic in one dimension and invariant in the other dimension so that a two-dimensional problem results. The incident field is a plane wave electrically polarized along the invariant direction of the configuration. However, the approach is capable of being generalized to arbitrary incidence and even 2D periodic structures. The arbitrarily chosen angle of incidence of the electric field lies in the transverse plane. As a consequence, Maxwell's equations in vectorial form reduce to a scalar differential equation in two dimensions. The solution of the scalar problem is expressed in an integral form using a regularized Green's function formulation. For the electric field we use a Floquet modal expansion, where the Floquet modal coefficients or reflection coefficients are written in terms of modified spatial Fourier transforms. These spatial Fourier transforms are solved in a closed form by using Green's second identity which transforms the surface integral into a boundary integral.

1.3 Outline of the thesis

This thesis is organized as follows. Chapter 2 is concerned with the formulation of scattering problems for the electric field for an arbitrary shaped object in free-space. In Chapter 3, we first consider the case of an infinitely long dielectric cylinder with triangular cross section embedded in free space. For this case, we demonstrate the feasibility of the assumed linear approximation of the electric field inside the object and of the proposed transformation techniques to obtain a closed form formulation. In Chapter 4, we use the methods developed in Chapter 3 to formulate the scattering problem for diffraction gratings which are periodic in one dimension. In Chapter 5, we validate the developed methods and we discuss a few representative numerical results. Finally, in Chapter 6 we discuss some conclusions and we recommend a solution strategy for three-dimensional diffraction gratings illuminated by an incident field with arbitrary polarization.

Chapter 2

Electromagnetic scattering problems

In this chapter we introduce Maxwell's equations, the constitutive relations and the boundary conditions to formulate electromagnetic field problems. We decompose Maxwell's equations in terms of longitudinal and transverse components from which we obtain a coupled system of differential equations for the electric field. For the resulting Helmholtz equations for the electric field components, a Green's function formulation is employed. Finally, using Green's function, we formulate the electric field in the form of a frequency-domain integral representation for an object embedded in free space.

2.1 Maxwell's equations

To investigate electromagnetic field problems we first have to choose the framework of formulation. In a historical perspective, going back to 1864, James Clerk Maxwell postulated nine equations related to electricity and magnetism which are nowadays qualified as the most complete theory of macroscopic electromagnetism. With the introduction of the vector notation, these equations can be written in a more convenient form from mathematical and physical point of view. Although electromagnetic field problems are more easily imaginable in the time domain, we consider the frequency domain representation since this reduces the complexity of the problem. Hence, a temporal Fourier transformation is used to transform the Maxwell equations to the frequency domain. The electromagnetic field is now dependent on the time by a complex time factor $\exp(-i\omega t)$ and the derivatives in the Maxwell equations reduces in a multiplication with a complex factor, i.e. $\partial_t \leftrightarrow -i\omega$.

The Maxwell equations in the space-frequency domain are given by [8]

$$\begin{aligned}
\nabla \times \mathbf{E}(\mathbf{r},\omega) &= i\omega\mathbf{B}(\mathbf{r},\omega) && (2.1a)\\
\nabla \times \mathbf{H}(\mathbf{r},\omega) &= \mathbf{J}(\mathbf{r},\omega) - i\omega\mathbf{D}(\mathbf{r},\omega) && (2.1b)\\
\nabla \cdot \mathbf{D}(\mathbf{r},\omega) &= \rho(\mathbf{r},\omega) && (2.1c)\\
\nabla \cdot \mathbf{B}(\mathbf{r},\omega) &= \mathbf{0} && (2.1d)
\end{aligned}$$

and the continuity equation or the charge conservation law is given by

$$\nabla \cdot \mathbf{J}(\mathbf{r}, \omega) = i\omega\rho(\mathbf{r}, \omega) \tag{2.2}$$

where the vectorial electromagnetic field quantities $\{\mathbf{E}(\mathbf{r}, \omega), \mathbf{H}(\mathbf{r}, \omega), \mathbf{D}(\mathbf{r}, \omega), \mathbf{B}(\mathbf{r}, \omega)\}$ are the electric field, magnetic field, electric flux density and the magnetic flux density, respectively. The sources of the electromagnetic fields are represented by the (external) source density $\mathbf{J}(\mathbf{r}, \omega)$ and the charge density $\rho(\mathbf{r}, \omega)$, where the latter is a scalar quantity. The electromagnetic fields are two times continuously differentiable [1] vector functions, i.e.

$$\{\mathbf{D}, \mathbf{E}, \mathbf{B}, \mathbf{H}\} \in C^2(\mathbb{R}^3) \tag{2.3}$$

where, from now on, we omit the explicit notation of the spatial and frequency dependence of the relevant (field and source) quantities.

To model the effects of electromagnetic fields in matter, we introduce the constitutive relations. These relations provide a basis to relate the fluxes **D** and **B** to the fields **E** and **H**, respectively. In the most general form, the constitutive relations are given by

$$\mathbf{D} = \bar{\epsilon}\mathbf{E} \tag{2.4a}$$

$$\mathbf{B} = \bar{\mu}\mathbf{H} \tag{2.4b}$$

where $\bar{\epsilon}$ and $\bar{\mu}$ denotes the permittivity and the permeability tensors with spatial dependency, respectively. Since in this thesis we consider media which are linear, isotropic and nondispersive, the constitutive tensors reduce to a constant which are dependent on the material properties, i.e. $\bar{\epsilon} = \epsilon_0\epsilon_r$ and $\bar{\mu} = \mu_0\mu_r$. The relative permittivity ϵ_r and the relative permeability μ_r are referenced to the free-space permittivity ϵ_0 and permeability μ_0. For objects embedded in a homogeneous background medium, for instance free space, the difference between $\{\mathbf{D}, \mathbf{B}\}$ in free space and $\{\mathbf{D}, \mathbf{B}\}$ in materials is important. Therefore, we may write the constitutive relations as

$$\mathbf{D} = \epsilon_0\mathbf{E} + \epsilon_0\chi_e\mathbf{E} \tag{2.5a}$$

$$\mathbf{B} = \mu_0\mathbf{H} + \mu_0\chi_m\mathbf{H} \tag{2.5b}$$

where the dimensionless electric and magnetic susceptibilities are defined as

$$\chi_e = \epsilon_r - 1 \qquad \text{and} \qquad \chi_m = \mu_r - 1 \tag{2.6}$$

respectively.

In addition, in optics it is common to relate the speed of light in free space to that in a medium by the refractive index, n. For electromagnetic waves, the relation between the wavelength in free space λ_0 and the wavelength in a dielectric medium λ_{mat} is derived from the relative permittivity as

$$\lambda_{\text{mat}} = \lambda_0/n \qquad \text{with} \qquad n = \sqrt{\epsilon_r}. \tag{2.7}$$

---

[1] $C^k(\Omega), k \in N \cup \{0\}$: The vector space of k-times continuously differentiable functions on Ω, with $C^0(\Omega) = C(\Omega)$ the vector space of continuous functions from Ω to R.

Finally, substituting Eq. (2.5) in the Maxwell equations (2.1) results in

$$\nabla \times \mathbf{E} - i\omega\mu_0\mathbf{H} = i\omega\mu_0\chi_m\mathbf{H} \tag{2.8a}$$

$$\nabla \times \mathbf{H} + i\omega\epsilon_0\mathbf{E} = \mathbf{J} + i\omega\epsilon_0\chi_e\mathbf{E}. \tag{2.8b}$$

In order to get Maxwell equations which are well-posed, additional requirements have to be set for the field quantities at the boundaries between media with different electromagnetic properties. Therefore we introduce the boundary conditions at the interface between two adjacent regions D_1 and D_2. From Maxwell's equations we can easily derive the boundary conditions for the electric and magnetic field as

$$\mathbf{n}_{12} \times (\mathbf{E}_1 - \mathbf{E}_2) = \mathbf{0} \tag{2.9}$$

$$\mathbf{n}_{12} \times (\mathbf{H}_1 - \mathbf{H}_2) = \mathbf{J}_s \tag{2.10}$$

where the normal $\mathbf{n}_{12}$ is directed into domain D_2 and the subscript of the fields denotes the domain where the fields are evaluated.

A special case occurs when the boundary lies at infinity. For that case, the so-called Sommerfeld radiation conditions and the finiteness conditions apply, which are respectively given by

$$\lim_{||\mathbf{r}|| \to \infty} ||\mathbf{r}|| \{E(\mathbf{r}) - Z_0 \boldsymbol{n} \times H(\mathbf{r})\} = o(1) \tag{2.11}$$

$$\lim_{||\mathbf{r}|| \to \infty} \{E(\mathbf{r}), H(\mathbf{r})\} = O(\frac{1}{||\mathbf{r}||}) \tag{2.12}$$

where the asymptotic behavior is denoted by the Landau order symbol O and Z_0 is the impedance of free space.

2.2 Transverse-longitudinal field decomposition

For objects which are invariant along the y-coordinate, we will decompose the vectorial quantities in Maxwell's equations. The relevant vectorial quantities will be represented as

$$\mathbf{E} = \mathbf{E}_T + E_y\mathbf{u}_y \tag{2.13}$$

$$\nabla = \nabla_T + \mathbf{u}_y\partial_y \tag{2.14}$$

and similar definitions for other quantities. The transverse components, denoted by the subscript $_T$, lie in the (x, z)-plane and the longitudinal components are in the y-direction. We assume that the fields are derived in free space, so that the electric and magnetic susceptibility vanish, i.e. $\chi_e = \chi_m = 0$. With this assumption and substituting Eqs. (2.13-2.14) in Eq. (2.8) we obtain the following expressions

$$(\nabla_T + \mathbf{u}_y\partial_y) \times (\mathbf{E}_T + E_y\mathbf{u}_y) - i\omega\mu_0(\mathbf{H}_T + H_y\mathbf{u}_y) = \mathbf{0} \tag{2.15}$$

$$(\nabla_T + \mathbf{u}_y\partial_y) \times (\mathbf{H}_T + H_y\mathbf{u}_y) + i\omega\epsilon_0(\mathbf{E}_T + E_y\mathbf{u}_y) = \mathbf{J}_T + J_y\mathbf{u}_y. \tag{2.16}$$

The partial derivative with respect to the y-direction, ∂_y, will be rewritten in an algebraic form by using a spatial transform since the configuration is invariant in the y-direction. We define the forward and inverse spatial Fourier transform pair as

$$\begin{aligned} \hat{E}_y(x,z,k_y) &= \int_{-\infty}^{\infty} \exp(-ik_y y)E_y(x,z,y)dy && (2.17) \\ E_y(x,z,y) &= \frac{1}{2\pi}\int_{-\infty}^{\infty} \exp(ik_y y)\hat{E}_y(x,z,k_y)dk_y && (2.18) \end{aligned}$$

which are in accordance with the temporal Fourier transform. Using Eq. (2.17), the partial derivatives in Eqs. (2.13-2.14) will be replaced by an algebraic factor, i.e. $\partial_y \leftrightarrow ik_y$, and we find the following coupled system of equations

$$\begin{aligned} \nabla_T \times \hat{\mathbf{E}}_T &= i\omega\mu_0\hat{H}_y\mathbf{u}_y && (2.19) \\ \nabla_T \times \hat{E}_y\mathbf{u}_y + \mathbf{u}_y \times ik_y\hat{\mathbf{E}}_T &= i\omega\mu_0\hat{\mathbf{H}}_T && (2.20) \\ \nabla_T \times \hat{\mathbf{H}}_T &= \hat{J}_y\mathbf{u}_y - i\omega\epsilon_0\hat{E}_y\mathbf{u}_y && (2.21) \\ \nabla_T \times \hat{H}_y\mathbf{u}_y + \mathbf{u}_y \times ik_y\hat{\mathbf{H}}_T &= \hat{\mathbf{J}}_T - i\omega\epsilon_0\hat{\mathbf{E}}_T. && (2.22) \end{aligned}$$

We proceed by eliminating $\{\hat{\mathbf{H}}_T, \hat{H}_y\}$ and rewriting $\{\hat{\mathbf{E}}_T, \hat{E}_y\}$ in terms of $\{\hat{\mathbf{J}}_T, \hat{J}_y\}$. To this end, we take the transverse curl of Eq. (2.19)

$$\begin{aligned} \nabla_T \times \nabla_T \times \hat{\mathbf{E}}_T &= i\omega\mu_0\nabla_T \times \hat{H}_y\mathbf{u}_y && (2.23) \\ &= i\omega\mu_0\{\hat{\mathbf{J}}_T - i\omega\epsilon_0\hat{\mathbf{E}}_T - ik_y\mathbf{u}_y \times \hat{\mathbf{H}}_T\} && (2.24) \end{aligned}$$

where we have used Eq. (2.22). Substituting Eq. (2.20) in the right-hand side of Eq. (2.24) results in

$$\nabla_T \times \nabla_T \times \hat{\mathbf{E}}_T = i\omega\mu_0\{\hat{J}_y - i\omega\epsilon_0\hat{\mathbf{E}}_T\} - ik_y\mathbf{u}_y \times \{\nabla_T \times \hat{E}_y\mathbf{u}_y + \mathbf{u}_y \times ik_y\hat{\mathbf{E}}_T\}. \qquad (2.25)$$

With the use of the following identities

$$\begin{aligned} \mathbf{u}_y \times (\nabla_T \times \mathbf{u}_y)\hat{E}_y &= \underbrace{(\mathbf{u}_y \cdot \mathbf{u}_y)}_{1}\nabla_T\hat{E}_y - \underbrace{(\mathbf{u}_y \cdot \nabla_T)}_{0}\mathbf{u}_y\hat{E}_y && (2.26) \\ \mathbf{u}_y \times (\mathbf{u}_y \times \hat{\mathbf{E}}_T) &= \underbrace{(\mathbf{u}_y \cdot \hat{\mathbf{E}}_T)}_{0}\mathbf{u}_y - \underbrace{(\mathbf{u}_y \cdot \mathbf{u}_y)}_{1}\hat{\mathbf{E}}_T && (2.27) \\ \nabla_T \times \nabla_T \times \hat{\mathbf{E}}_T &= \nabla_T(\nabla_T \cdot \hat{\mathbf{E}}_T) - \nabla^2\hat{\mathbf{E}}_T && (2.28) \end{aligned}$$

Eq. (2.25) reduces to

$$\nabla_T(\nabla_T \cdot \hat{\mathbf{E}}_T) - \nabla^2\hat{\mathbf{E}}_T = i\omega\mu_0\hat{\mathbf{J}}_T + \omega^2\epsilon_0\mu_0\hat{\mathbf{E}}_T - ik_y\nabla_T\hat{E}_y - k_y^2\hat{\mathbf{E}}_T. \qquad (2.29)$$

In the latter expression, the term with $\nabla_T \cdot \hat{\mathbf{E}}_T$ is inconvenient so that we use Eq. (2.22) and (2.21) to rewrite this term

$$\begin{aligned} ik_y\nabla_T \cdot (\mathbf{u}_y \times \hat{\mathbf{H}}_T) &= \nabla_T \cdot \hat{\mathbf{J}}_T - i\omega\epsilon_0\nabla_T \cdot \hat{\mathbf{E}}_T && (2.30) \\ -ik_y\mathbf{u}_y \cdot (\nabla_T \times \hat{\mathbf{H}}_T) &= -ik_y(\hat{J}_y - i\omega\epsilon_0\hat{E}_y). && (2.31) \end{aligned}$$

Successively, we find for the gradient-divergence operator

$$\nabla_T \cdot \hat{\mathbf{E}}_T = \frac{1}{i\omega\epsilon_0}\{(\nabla_T \cdot \hat{\mathbf{J}}_T) + ik_y(\hat{J}_y - i\omega\epsilon_0\hat{E}_y)\} \tag{2.32}$$

$$\nabla_T(\nabla_T \cdot \hat{\mathbf{E}}_T) = \frac{1}{i\omega\epsilon_0}\nabla_T(\nabla_T \cdot \hat{\mathbf{J}}_T) + \frac{k_y}{\omega\epsilon_0}\nabla_T\hat{J}_y - ik_y\nabla_T\hat{E}_y. \tag{2.33}$$

Finally, substituting Eq. (2.33) in Eq. (2.29) results in the 2D Helmholtz equation for $\hat{\mathbf{E}}_T$

$$\{\nabla_T^2 + (\omega^2\epsilon_0\mu_0 - k_y^2)\}\hat{\mathbf{E}}_T = \frac{1}{i\omega\epsilon_0}\{\nabla_T\nabla_T \cdot + \omega^2\epsilon_0\mu_0\}\hat{\mathbf{J}}_T + \frac{k_y}{\omega\epsilon_0}\nabla_T\hat{J}_y \tag{2.34}$$

where $\hat{\mathbf{E}}_T$ is expressed in terms of $\hat{J}_y$ and $\hat{\mathbf{J}}_T$.

A similar 2D Helmholtz equation for $\hat{E}_y$ can now be derived in the same manner. The resulting expression is found as

$$\{\nabla_T^2 + (\omega^2\epsilon_0\mu_0 - k_y^2)\}\hat{E}_y = \frac{1}{i\omega\epsilon_0}(\omega^2\epsilon_0\mu_0 - k_y^2)\hat{J}_y + \frac{k_y}{\omega\epsilon_0}\nabla_T \cdot \hat{\mathbf{J}}_T \tag{2.35}$$

where $\hat{E}_y$ is now expressed in terms of $\hat{J}_y$ and $\hat{\mathbf{J}}_T$.

2.3 Scalar and vector potentials

In order to find a solution for $\hat{\mathbf{E}}_T$ and $\hat{E}_y$ in Eqs. (2.34-2.35), we employ a Green's function formulation. We define Green's function G_0 as the point source solution of the following scalar wave equation

$$\{\nabla_T^2 - \gamma^2)\}G_0(\mathbf{r}_T, \mathbf{r}'_T) = -\delta(\mathbf{r}'_T - \mathbf{r}_T) \qquad \mathbf{r}_T \in \mathbb{R}^2 \tag{2.36}$$

that satisfies the radiation condition as $|\mathbf{r}_T| \to \infty$. This function is given by

$$G_0(\mathbf{r}_T, \mathbf{r}'_T) = \frac{1}{2\pi}K_0(\gamma|\mathbf{r}'_T - \mathbf{r}_T|) \tag{2.37}$$

where δ is the Dirac delta distribution representing a point source located in $\mathbf{r}'_T$. In Eq. (2.37) the axial wave number is found as $\gamma^2 = k_y^2 - \omega^2\epsilon\mu_0$ and K_0 is the zero-order modified Bessel function of the second kind. The modified Bessel function (of the second kind) can be written as a Hankel function using the relation

$$H_\alpha^{(1)}(\rho) = \frac{2}{\pi}i^{-(\alpha+1)}K_\alpha(i\rho) \tag{2.38}$$

where α is the order of the Bessel function. By including the effects of a general source term $\hat{\mathbf{J}}_T$ at the right-hand side of Eq. (2.36), the wave equation results in

$$(\nabla_T^2 - \gamma^2)\mathbf{A}(\mathbf{r}_T) = \hat{\mathbf{J}}_T \tag{2.39}$$

where $\mathbf{A}(\mathbf{r}_T)$ is a vector potential. Owing to the superposition principle, we combine the results of Eq. (2.36) and (2.37) to obtain the solution of Eq. (2.39) as

$$\mathbf{A}(\mathbf{r}_T) = -\iint_{D_\infty} G_0(\mathbf{r}_T, \mathbf{r}'_T)\hat{\mathbf{J}}_T(\mathbf{r}'_T)dA' \tag{2.40}$$

where the domain of integration D_∞ is unbounded so that the current distribution specifies the domain of integration. Similar reasoning apply for the source term, $\hat{J}_y$. Hence we find

$$\begin{aligned} (\nabla_T^2 - \gamma^2)\Psi(\mathbf{r}_T) &= \hat{J}_y && (2.41) \\ \Psi(\mathbf{r}_T) &= -\iint_{D_\infty} G_0(\mathbf{r}_T, \mathbf{r}'_T)\hat{J}_y(\mathbf{r}'_T)dA' && (2.42) \end{aligned}$$

where $\Psi(\mathbf{r}_T)$ is a scalar potential. Finally, with the found potentials we can express $\hat{\mathbf{E}}_T$ and $\hat{E}_y$ as

$$\begin{aligned} \hat{\mathbf{E}}_T(\mathbf{r}_T) &= \frac{-1}{i\omega\epsilon_0}(\nabla_T\nabla_T \cdot + \omega^2\epsilon_0\mu_0)\mathbf{A}(\mathbf{r}_T) - \frac{k_y}{\omega\epsilon_0}\nabla_T\Psi(\mathbf{r}_T) && (2.43) \\ \hat{E}_y(\mathbf{r}_T) &= \frac{-1}{i\omega\epsilon_0}(\omega^2\epsilon_0\mu_0 - k_y^2)\Psi(\mathbf{r}_T) - \frac{k_y}{\omega\epsilon_0}(\nabla_T \cdot \mathbf{A}(\mathbf{r}_T)) && (2.44) \end{aligned}$$

where the scalar and the vector potentials Ψ and $\mathbf{A}$ are written in terms of Green's function, respectively.

2.4 Integral representation

In the previous section we derived expressions for the electric fields in free space, in terms of potentials. In this section we discuss the effects of non-magnetic objects embedded in free space in the framework of scattering problems. Hence, we consider free space as the background medium and the object as the scatterer. The inclusion of a medium with dielectric properties means that the permitivity now depends on the position, i.e. $\epsilon(\mathbf{r}_T) \geq \epsilon_0$. For this case, Maxwell's equations for the total field are given by

$$\begin{aligned} \nabla \times \mathbf{E} - i\omega\mu_0\mathbf{H} &= \mathbf{0} && (2.45) \\ \nabla \times \mathbf{H} + i\omega\epsilon_0\mathbf{E} &= \mathbf{J} - i\omega\epsilon_0\chi_e(\mathbf{r}_T)\mathbf{E} && (2.46) \end{aligned}$$

with $\chi_e(\mathbf{r}_T) = \epsilon_r(\mathbf{r}_T) - 1$ dependent on the position $\mathbf{r}_T$.

We assume that the source term $\mathbf{J}$ is an impressed current which means that we may write the incident field $\{\hat{\mathbf{E}}^i, \hat{\mathbf{H}}^i\}$ as

$$\begin{aligned} \nabla \times \mathbf{E}^i - i\omega\mu_0\mathbf{H}^i &= \mathbf{0} && (2.47) \\ \nabla \times \mathbf{H}^i + i\omega\epsilon_0\mathbf{E}^i &= \mathbf{J}. && (2.48) \end{aligned}$$

The total field is defined as the sum of the incident field and of the secondary or scattered field

$$\{\mathbf{E}, \mathbf{H}\} = \{\mathbf{E}^i, \mathbf{H}^i\} + \{\mathbf{E}^s, \mathbf{H}^i\}. \tag{2.49}$$

As a consequence of the linearity of the Maxwell equations, we may subtract Eq. (2.47) from (2.45) to find the equation governing the scattered field $\{\hat{\mathbf{E}}^s, \hat{\mathbf{H}}^s\}$

$$\begin{aligned} \nabla \times \mathbf{E}^s - i\omega\mu_0\mathbf{H}^s &= \mathbf{0} && (2.50)\\ \nabla \times \mathbf{H}^s + i\omega\epsilon_0\mathbf{E}^s &= -i\omega\epsilon_0\chi_e(\mathbf{r}_T)\mathbf{E}. && (2.51) \end{aligned}$$

The term at the right-hand side of Eq. (2.51) is recognized as a Fourier transformed polarization term or, in the context of scattering problems, as an induced contrast source and given by

$$\begin{aligned} \mathbf{J}_T(\mathbf{r}_T) &= -i\omega\epsilon_0\chi_e(\mathbf{r}_T)\mathbf{E}_T && (2.52)\\ J_y(\mathbf{r}_T) &= -i\omega\epsilon_0\chi_e(\mathbf{r}_T)E_y. && (2.53) \end{aligned}$$

Since the support of the polarization term is localized in a finite domain, the scattered field satisfies the radiation and causality conditions so that the potential evaluated over an unbounded domain as discussed in the previous section can be used. The electric field expressed in terms of potentials are thus applicable.

Using the induced contrast source term, we define the scaled potentials as

$$\begin{aligned} \mathbf{A}^s(\mathbf{r}_T) &= \frac{-1}{i\omega\epsilon_0}\mathbf{A}(\mathbf{r}_T) && (2.54)\\ &= \iint_{D_\infty} G_0(\mathbf{r}_T, \mathbf{r}_T')\chi_e(\mathbf{r}_T')\hat{\mathbf{E}}_T(\mathbf{r}_T')dA' && (2.55) \end{aligned}$$

and

$$\begin{aligned} \Psi^s(\mathbf{r}_T) &= \frac{-1}{i\omega\epsilon_0}\Psi(\mathbf{r}_T) && (2.56)\\ &= \iint_{D_\infty} G_0(\mathbf{r}_T, \mathbf{r}_T')\chi_e(\mathbf{r}_T')\hat{E}_y(\mathbf{r}_T')dA'. && (2.57) \end{aligned}$$

In a similar manner we express the scattered electric field in terms of the above given potentials, i.e.

$$\begin{aligned} \hat{\mathbf{E}}_T^s(\mathbf{r}_T) &= (\nabla_T\nabla_T\cdot + \omega^2\epsilon_0\mu_0)\mathbf{A}^s(\mathbf{r}_T) + ik_y\nabla_T\Psi^s(\mathbf{r}_T) && (2.58a)\\ \hat{E}_y^s(\mathbf{r}_T) &= (\omega^2\epsilon_0\mu_0 - k_y^2)\Psi^s(\mathbf{r}_T) - ik_y(\nabla_T \cdot \mathbf{A}^s(\mathbf{r}_T)). && (2.58b) \end{aligned}$$

When applying the boundary conditions on Eq. (2.58a), one can shown that the tangential component of the electric field is continuous across the interface between the two media. For the normal component, the right-hand side of Eq.(2.58a) is discontinuous so that in Eq. (2.58a) we consider rewriting the $\nabla_T\nabla_T\cdot$ term. We use the following identity

$$\nabla_T(\nabla_T \cdot \mathbf{A}^s) = \nabla_T \times \nabla_T \times \mathbf{A}^s + \nabla_T^2\mathbf{A}^s. \qquad (2.59)$$

With the definitions of the potential $\mathbf{A}^s$ and of the Green's function G_0, we write the term at the right-hand side of Eq. (2.59) as

$$\begin{aligned}
\nabla_T^2\mathbf{A}^s &= \iint_{D_\infty} \nabla_T^2 G_0(\mathbf{r}_T,\mathbf{r}_T')\chi_e(\mathbf{r}_T')\hat{\mathbf{E}}_T(\mathbf{r}_T')dA' \\
&= \iint_{D_\infty} (k_y^2-\omega^2\epsilon_0\mu_0)G_0(\mathbf{r}_T,\mathbf{r}_T')\chi_e(\mathbf{r}_T')\hat{\mathbf{E}}_T(\mathbf{r}_T')dA' \\
&\qquad -\iint_{D_\infty} \delta(\mathbf{r}_T'-\mathbf{r}_T)G_0(\mathbf{r}_T,\mathbf{r}_T')\chi_e(\mathbf{r}_T')\hat{\mathbf{E}}_T(\mathbf{r}_T')dA' \\
&= (k_y^2-\omega^2\epsilon_0\mu_0)\mathbf{A}^s(\mathbf{r}_T)-\chi_e(\mathbf{r}_T)\hat{\mathbf{E}}_T(\mathbf{r}_T)
\end{aligned} \tag{2.60}$$

Substituting Eq. (2.60) in (2.58a) results in

$$\frac{\epsilon}{\epsilon_0}\hat{\mathbf{E}}_T(\mathbf{r}_T)-\hat{\mathbf{E}}_T^i(\mathbf{r}_T)=(\nabla_T\times\nabla_T\times+k_y^2)\mathbf{A}^s(\mathbf{r}_T)-ik_y\nabla_T\Psi^s(\mathbf{r}_T). \tag{2.61}$$

The electric field is now fully specified by Eqs. (2.58) and (2.61). Because of the choice of Green's function, the left-hand side of (2.61) represents an outgoing or scattered field as $|\mathbf{r}_T|\to\infty$. In the next chapter we will use these equations to formulate the scattered electric field for an infinitely long dielectric cylinder with triangular cross section illuminated by an electrically polarized plane wave.

Chapter 3

Non-periodic dielectric cylinder

In this chapter we consider the scattering of an electrically polarized plane wave by an infinity long dielectric cylindrical object with triangular cross section. In this scattering problem, the unknown electric field inside the object is determined with the aid of an integral equation, as derived in Chapter 2. We assume that the wavelength of the electric field inside the object is large compared to the dimensions of the cross section of the cylinder. Therefore, the electric field inside the object may be expanded in terms of linear basis functions. With the use of the linear functions, we reduce the integral over the surface of the object to a contour integral along the boundary of the object [13]. The result is a closed-form expression for the integral equation. We apply the point matching method, a special case of the method of moments, to solve the integral equation from which the electric field inside the object is found. Finally, we formulate the scattered electric far field, where we use Green's second identity to obtain a closed-form representation.

3.1 Electric field in cylinder with triangular cross section

The problem to be solved is the calculation of the scattered electric field due to an electrically polarized plane wave with an arbitrary angle of incidence in the presence of an infinitely long dielectric cylinder with triangular cross section (see Fig. 3.1) [13]. We assume that the configuration has infinite length along the longitudinal direction i.e. the y-coordinate and that the transverse cross section is in the (x-z)-plane. The domain D of the object consist of a homogeneous dielectric material with permittivity ϵ_{mat} and permeability μ_0, while the embedding is free space with permittivity ϵ_0 and permeablility μ_0. The incident electric field with time dependence $\exp(-i\omega t)$ is directed along the y-coordinate, i.e. $\mathbf{E}^p(\mathbf{r}) = E^p_y(\mathbf{r})\mathbf{u}_y$.

Since the incident field is polarized in the y-direction and has no spatial dependence on the invariant direction of the configuration, the coupling in the system of equations in Eq. (2.58) vanishes. This means that for the total electric field the following domain integral equation is found

$$E_y(\mathbf{r}_T) = E^p_y(\mathbf{r}_T) + k_0^2 \iint_D G_0(\mathbf{r}_T, \mathbf{r}'_T)\chi_e(\mathbf{r}'_T)E_y(\mathbf{r}'_T)dA' \tag{3.1}$$

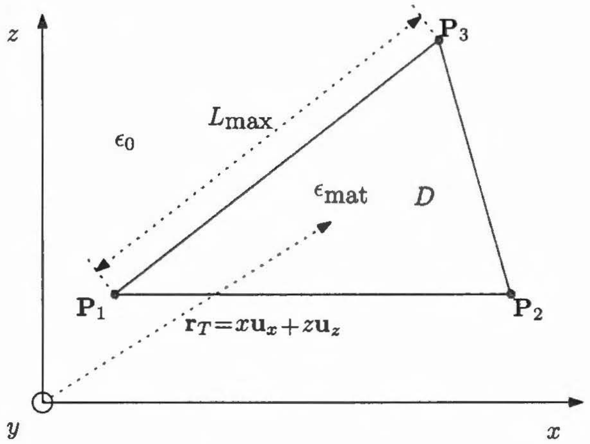

Figure 3.1: Transverse cross section of an object embedded in free space.

where $\mathbf{r}_T = (x, z)$ represents the spatial position. The free-space wave number is $k_0 = \omega\sqrt{\epsilon_0\mu_0}$ and $\chi_e(\mathbf{r}_T)$ is the contrast function which is $\chi_e = (\epsilon_{\text{mat}}/\epsilon_0) - 1$ for $\mathbf{r}_T \in D$ and zero elsewhere. Green's function G_0 in Eq. (3.1) is defined as

$$G_0(\mathbf{r}_T, \mathbf{r}'_T) = \frac{1}{2\pi} K_0(\gamma|\mathbf{r}'_T - \mathbf{r}_T|) \quad \text{with} \quad \gamma^2 = k_y^2 - k_0^2 \tag{3.2}$$

where K_0 denotes the zero-order modified Bessel function of the second kind. The axial wave number reduces then to $\gamma = -ik_0$ since the incident field and the configuration are invariant in the y-direction, i.e. $k_y = 0$.

We define the maximum dimension of the object $L_{\max}$ as

$$L_{\max} = \max_{i=1,3,j=1,3} ||\mathbf{P}_i - \mathbf{P}_j|| \quad \text{with} \quad (\mathbf{P}_i, \mathbf{P}_j) \in \mathbb{R}^2 \tag{3.3}$$

where $(\mathbf{P}_i, \mathbf{P}_j)$ are the vertex positions of the object and $||.||$ is the Euclidean norm representing the distance between the vertex positions, see Fig. 3.1.

We assume that the wavelength of the electric field inside the object λ_{mat} is considerably larger than the maximum dimension of the object, namely $L_{\max} < 0.25\lambda_{\text{mat}}$. This means that, locally, the electric field is approximately linear such that we can consider it as a quasi-static field. Therefore we may use a small-argument approximation for the modified Bessel function K_0 in Eq. (3.2)

$$K_0(y) \approx -\{\ln(y/2) + \varepsilon\} \quad \text{if} \quad y \ll 1 \tag{3.4}$$

where ε denotes Eulers constant [9]. By substituting Eq. (3.4) in Eq. (3.1), the following expression for the total electric field is found as

$$E_y(\mathbf{r}_T) = E_y^p(\mathbf{r}_T) + k_0^2 \iint_D -[\ln(\frac{\gamma}{2}|\mathbf{r}'_T - \mathbf{r}_T|) + \varepsilon]\chi_e(\mathbf{r}'_T)E_y(\mathbf{r}'_T)dA' \tag{3.5}$$

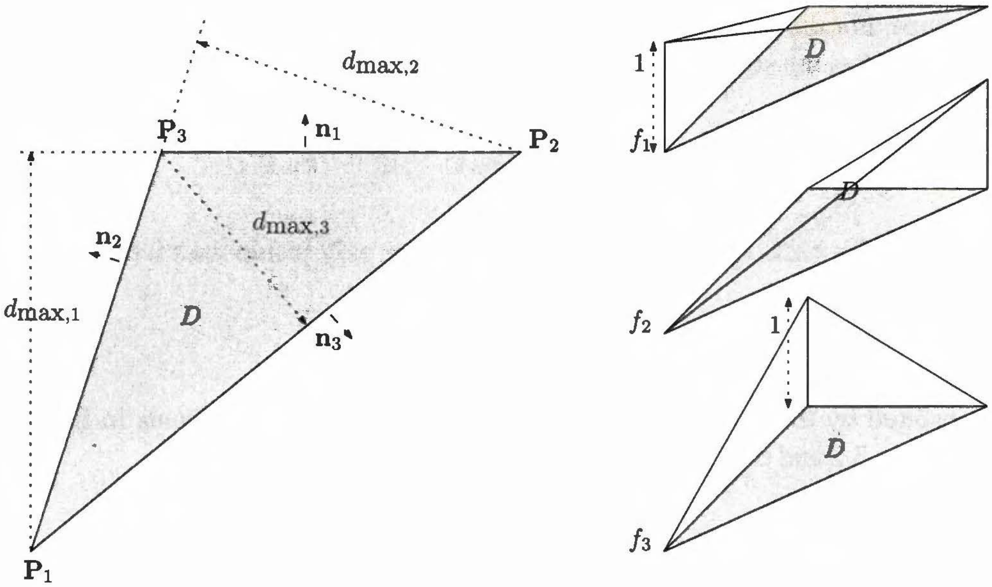

Figure 3.2: Variables definitions for the basis functions and the three basis functions defined for triangular domain D.

As shown in Eq. (3.5), when the observation position $\mathbf{r}_T$ and the integration variable $\mathbf{r}'_T$ coincide, the integrand becomes singular. This is a consequence of the singular behavior of Green's function when the distance function $(|\mathbf{r}'_T - \mathbf{r}_T|)$ becomes zero. Therefore we consider rewriting the integrand of Eq. (3.5) in a regular part and a singular part. The integral over the 2D domain with singular integrand can be solved analytically. Similar arguments apply for the integral over the 2D domain with regular integrand. By applying the discussed solution method, the electric field is found as

$$E_y(\mathbf{r}_T) = E_y^p(\mathbf{r}_T) + \frac{k_0^2\chi_e}{2\pi}[I_{\text{reg}} + I_{\text{sing}}(\mathbf{r}_T)] \tag{3.6}$$

with

$$\begin{aligned} I_{\text{reg}} &= \{\ln(2/\gamma) - \varepsilon\} \iint_D E_y(\mathbf{r}'_T)dA' && (3.7) \\ I_{\text{sing}}(\mathbf{r}_T) &= \iint_D \ln(|\mathbf{r}'_T - \mathbf{r}_T|)E_y(\mathbf{r}'_T)dA' && (3.8) \end{aligned}$$

where we have written the kernel of the surface integral in Eq. (3.5) as a sum of a regular part and a singular part, which leads to two domain integrals.

3.1.1 Triangular basis functions

In the foregoing section we have assumed that the electric field inside the object is quasi-static. Therefore, we may approximate the total electric field inside the object using a combination of linear functions. For the given domain of the object, we use triangular basis functions. The total field is then found as the sum of weighted basis functions, i.e.

$$E_y(\mathbf{r}_T) = \sum_{j=1}^{3} \hat{E}_{y,j} f_j(\mathbf{r}_T) \qquad \text{if} \qquad \mathbf{r}_T \in D \tag{3.9}$$

where the triangular basis functions f_j that have support only inside the triangular domain and they are defined as

$$f_j(\mathbf{r}_T) = \left[1 - \frac{\mathbf{n}_j \cdot (\mathbf{r}_T - \mathbf{r}_{T,j})}{d_{\max,j}}\right] \tag{3.10}$$

which is inspired by the RWG functions [14]. The variables and constants in Eq. (3.10) are presented in Fig. 3.2 and they represent the following quantities

$$\begin{aligned} \hat{E}_{y,j} &\;-\; \text{field amplitudes at vertex } \mathbf{P}_j, \qquad \forall_j \\ d_{\max,j} &= \mathbf{n}_j \cdot (\mathbf{r}_{T,i} - \mathbf{r}_{T,j}), \qquad \forall j \neq i \\ &\;-\; \text{length of vertex } j \text{ to edge } j \\ \mathbf{r}_{T,j} &\;-\; \text{position of vertex } \mathbf{P}_j \\ \mathbf{n}_j &\;-\; \text{outward pointing normal on edge} j \end{aligned}$$

where the edge j is the line segment located opposite to the vertex $\mathbf{P}_j$. The value of each basis function f_j is 1 at the particular vertex $\mathbf{P}_j$ and 0 at the other vertex positions as shown at the right of Fig. 3.2.

The fundamental unknowns are the weighting field amplitudes $\hat{E}_{y,j}$ in Eq. (3.9). Once the unknowns $\hat{E}_{y,j}$ are found, the resulting field outside the object is calculated by using Eq. (3.6) and (3.9) as an integral representation of the electric field in the whole space.

3.1.2 Surface integral to boundary integral transformation

Next, we will evaluate the integral with singular kernel in Eq. (3.8) in a closed form [13]. Substitution of Eq.(3.9) in (3.8) shows that the domain integral occurs in the following form

$$\iint_D g(\mathbf{r}_T) \ln(r_T) dA \tag{3.11}$$

where $g(\mathbf{r}_T) = \mathcal{L} \in \text{span}\{1, \mathbf{r}_T\}$ and $r_T = \sqrt{x^2 + z^2}$. Since we consider an object with piecewise straight lines as boundaries, we will rewrite Eq. (3.11) in a closed form. For a defined volume V enclosed by a closed surface S and an open surface D with boundary ∂D we write

$$\iint_D \mathbf{u}_y \cdot (\nabla_T \times \mathbf{v}) dA = \oint_{\partial D} \mathbf{v} \cdot \boldsymbol{\tau} dl \tag{3.12}$$

$$\iiint_V \nabla_T v dV = \iint_s v \mathbf{n} dA \tag{3.13}$$

which are known as Stokes' theorem and Gauss' theorem, respectively. In Eqs. (3.12-3.13), v is a scalar function, $\mathbf{v}$ is a vector function and $\boldsymbol{\tau}$ is the vector tangent to the boundary ∂D and $\mathbf{n} = \boldsymbol{\tau} \times \mathbf{u}_y$.

First, in Eq. (3.11) we consider the logarithmic term proportional to $\ln(r_T)$. In order to use the Stokes' theorem in Eq. (3.12), we have to find an expression for the unknown vector field $\mathbf{v}$. Therefore we write the integrand at the left-hand side of Eq. (3.12) as

$$\mathbf{u}_y \cdot (\nabla_T \times \mathbf{v}) = \ln(r_T) = \frac{1}{r_T}\left(\frac{\partial(r_T v_\phi)}{\partial r_T} - \frac{\partial v_{r_T}}{\partial \phi}\right) \tag{3.14}$$

from which, by solving the partial differential equation in cylindrical coordinates, an expression for the unknown vector function $\mathbf{v}$ is found

$$\mathbf{v} = (\mathbf{u}_y \times \mathbf{r}_T)v_\phi \qquad \text{with} \quad v_\phi = \frac{1}{2}\ln(r_T) - \frac{1}{4}. \tag{3.15}$$

Then the surface integral in Eq. (3.12) reduces to a boundary integral

$$\oint_{\partial D} [\mathbf{u}_y \times \mathbf{r}_T][\frac{1}{2}\ln(r_T) - \frac{1}{4}] \cdot \boldsymbol{\tau} dl = \oint_{\partial D} [\mathbf{n} \cdot \mathbf{r}_T][\frac{1}{2}\ln(r_T) - \frac{1}{4}]dl. \tag{3.16}$$

In a similar manner, the term which is proportional to $\mathbf{r}_T \ln(r_T)$ in Eq. (3.11) can be found. For that we use Gauss' theorem where the integrand is written as

$$\mathbf{r}_T \ln(r_T) = \nabla_T(v) \tag{3.17}$$

from which the unknown scalar v is found as

$$v = \frac{1}{2}r_T^2\left[\ln(r_T) - \frac{1}{4}\right]. \tag{3.18}$$

By applying Gauss' theorem for a volume of unit thickness in the longitudinal direction and taking into account that the contribution of the two surfaces cancels because the normal are vectors pointing in opposite directions, the volume integral in Eq. (3.13) is reduced to a boundary integral

$$\oint_{\partial D} v\mathbf{n}dA. \tag{3.19}$$

The boundary integrals in Eq. (3.16) and (3.19) will now be divided into three line integrals, so that they can be written as a sum of line integrals, where at each line the tangent and the normal vectors are constant. To make use of these constant vectors, the position vector $\mathbf{r}_T$ along a straight line segment is defined as

$$\mathbf{r}_T = (\mathbf{r}_T \cdot \mathbf{n})\mathbf{n} + (\mathbf{r}_T \cdot \boldsymbol{\tau})\boldsymbol{\tau} = d\mathbf{n} + s\boldsymbol{\tau} \tag{3.20}$$

where d is a constant and s is a coordinate along one particular line segment, see Fig. 3.3.

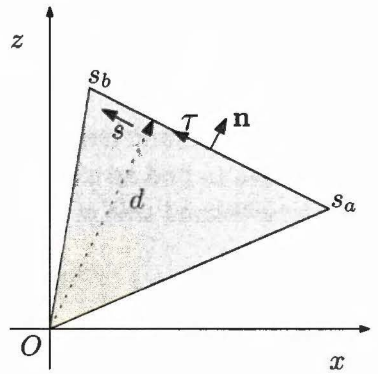

Figure 3.3: Parameterization definitions.

For each line segment we cast the integrals occurring in Eq. (3.16) and (3.19) in the following standard form

$$I_n(s_{a,l}, s_{b,l}; d) = \int_{s_{a,l}}^{s_{b,l}} s^n[\ln(s^2 + d^2) - 1]ds \tag{3.21}$$

where $s_{a,l}$ and $s_{b,l}$ denote the begin and the end positions on the line segment l, respectively. They are defined as

$$s_{a,l} = \tau_l \cdot \mathbf{r}_{T,l+1} \tag{3.22}$$

$$s_{b,l} = \tau_l \cdot \mathbf{r}_{T,l+2} \tag{3.23}$$

with $\{l+1, l+2\} = \text{modulo}(., 3)$.

Finally, the integral with logarithmic kernel over the 2D domain, in Eqs. (3.16) and (3.19), is rewritten as a linear combination of line integrals

$$\iint_D \ln(r_T)dA = \sum_{l=1}^{3} \frac{d_{\max,l}}{4} I_0(s_{a,l}, s_{b,l}; d_{\max,l}) \tag{3.24}$$

$$\begin{aligned} \iint_D \mathbf{r}_T \ln(r_T)dA &= \sum_{l=1}^{3} \frac{1}{4}\mathbf{n}_l[d^2_{\max,l} I_0(s_{a,l}, s_{b,l}; d_{\max,l}) \\ &\quad + I_2(s_{a,l}, s_{b,l}; d_{\max,l})]. \end{aligned} \tag{3.25}$$

The primitives of the standard integrals I_0 and I_2 can be found in Appendix A.

3.1.3 Method of Moments

With the introduction of the triangular basis functions and the evaluation of the integral over a 2D domain in closed form, we are now able to solve the domain integral equation occurring in Eq. (3.6). Therefore we apply a special case of the method of moments, where we use Dirac delta functions as test functions [15]. This case is called the point matching method, since the solution is approximated at a discrete set of points in the domain of interest. To explain the point matching method we generalize Eq. (3.6) into the following equation

$$E_y(\mathbf{r}_T) - L(E_y(\mathbf{r}_T)) = E_y^p(\mathbf{r}_T) \tag{3.26}$$

where L is the electric field integral operator defined inside the domain D. The total electric field in now expanded in terms of linear basis functions, as given in Eq. (3.9). Substituting Eq. (3.9) in left-hand side of Eq. (3.26) and taking at both sides the inner product with Dirac delta functions we obtain the following system of equations

$$\sum_{j=3} \langle f_j(\mathbf{r}_T) - L(f_j(\mathbf{r}_T)), \delta(\mathbf{r}_T - \mathbf{r}_{T,i}) \rangle = \langle E_y^p(\mathbf{r}_T), \delta(\mathbf{r}_T - \mathbf{r}_{T,i}) \rangle \quad \text{for} \quad i \in (1,3) \tag{3.27}$$

where $\langle .,. \rangle$ denotes the inner product on domain D defined as

$$\langle g(\mathbf{r}_T), h(\mathbf{r}_T) \rangle = \int_D g(\mathbf{r}_T) h(\mathbf{r}_T) d\mathbf{r}_T. \tag{3.28}$$

For this point matching method, the integral equation reduces to a system of linear equations. This system of equations from which the field amplitudes $\hat{E}_y$ have to be found can be solved by matrix inversion. The points where the electric field is approximated are called collocation points and are indicated by the subscript i i.e. $\mathbf{r}_{T,i}$. Therefore, the aim is to find a solution for total electric field at the collocation points.

Next, we will formulate the matrix elements in Eq. (3.27) in a closed form

$$E_y(\mathbf{r}_{T,i}) - \frac{k_0^2 \chi_e}{2\pi} [I_{\text{reg}} + I_{\text{sing}}(\mathbf{r}_{T,i})] = E_y^p(\mathbf{r}_{T,i}) \tag{3.29}$$

where I_{reg} and $I_{\text{sing}}(\mathbf{r}_{T,i})$ are defined in Eq. (3.7) and (3.8), respectively.

First, we consider the integral with singular kernel

$$I_{\text{sing}}(\mathbf{r}_{T,i}) = \iint_D \ln(|\mathbf{r}'_{T,i} - \mathbf{r}_T|) E_y(\mathbf{r}'_T) dA'. \tag{3.30}$$

Substituting Eq. (3.9) and (3.10) in the above equation leads to

$$\iint_D \ln(|\mathbf{r}'_T - \mathbf{r}_{T,i}|) E_y(\mathbf{r}'_T) dA' = \sum_{j=1}^{3} \hat{E}_{y,j} \iint_D \left[(1 + \frac{\mathbf{n}_j \cdot \mathbf{r}_{T,j}}{d_{\max,j}} - \frac{\mathbf{n}_j \cdot \mathbf{r}'_T}{d_{\max,j}}) \right] \ln(|\mathbf{r}'_T - \mathbf{r}_{T,i}|) dA'. \tag{3.31}$$

In order to make use of the expressions found in Eqs. (3.24-3.25) for the integral with singular kernel, we have to solve the problem of spatial discretization occurring at the right-hand side of Eq. (3.31). This problem is solved by rewriting the integrand in Eq. (3.24) and (3.25) as

$$(A + \mathbf{B} \cdot \mathbf{r}'_T) \ln(R_T) = \{(A + \mathbf{B} \cdot \mathbf{r}_{T,i}) + \mathbf{B} \cdot (\mathbf{r}'_T - \mathbf{r}_{T,i})\} \ln R_T \tag{3.32}$$

where $R_T = |\mathbf{r}'_T - \mathbf{r}_{T,i}|$ is the difference between the collocation vector position $\mathbf{r}_{T,i}$ and the vector position $\mathbf{r}'_T$, and $\{A, \mathbf{B}\}$ are an arbitrary chosen scalar and vector, respectively.

We proceed by casting the linear function in the kernel of Eq. (3.31) in the same form as the argument of the logarithmic function of the kernel, i.e.

$$\begin{gathered}\iint_D \ln(|\mathbf{r}_T' - \mathbf{r}_{T,i}|) E_y(\mathbf{r}_T') dA' = \\ \sum_{j=1}^{3} \hat{E}_{y,j} \iint_D \left[\left(1 + \frac{\mathbf{n}_j \cdot (\mathbf{r}_{T,j} - \mathbf{r}_{T,i})}{d_{\max,j}}\right) - \frac{\mathbf{n}_j}{d_{\max,j}} \cdot (\mathbf{r}_T' - \mathbf{r}_{T,i})\right] \ln(|\mathbf{r}_T' - \mathbf{r}_{T,i}|) dA'. \end{gathered} \quad (3.33)$$

In the above equation, we recognize the linear function in front of the logarithmic function as the sum of a constant term which does not depend on the integration variable and of a linear term which depends on the integration variable. Analog to the solving strategy used in Section 3.1.2, we first consider the case where the integrand is proportional to the logarithmic function $\ln(|\mathbf{r}_T' - \mathbf{r}_{T,i}|)$. Omitting the constants in Eq. (3.33), we transform the integral over surface D into an integral along the boundary of D. The integral over surface D with logarithmic kernel will now be written in a sum of line integrals corresponding to the line segments of the boundary of the object

$$\iint_D \ln(|\mathbf{r}_T' - \mathbf{r}_{T,i}|) dA' = \sum_{l=1}^{3} \left[\frac{(d_{\max,l} - d_{\mathrm{col},il})}{4}\right] I_0(s_{a,l} - s_{\mathrm{col},il}, s_{b,l} - s_{\mathrm{col},il}; d_{\max,l} - d_{\mathrm{col},il}) \quad (3.34)$$

where the standard integrals I_n are used, defined in Eq. (3.21). The collocation points, indicated by the subscript i, are parameterized in the local coordinate system relative to the line segment l, i.e.

$$s_{\mathrm{col},il} = \boldsymbol{\tau}_l \cdot (\mathbf{r}_{T,i} - \mathbf{r}_{T,l}) \quad (3.35)$$

$$d_{\mathrm{col},il} = \mathbf{n}_l \cdot (\mathbf{r}_{T,i} - \mathbf{r}_{T,l}). \quad (3.36)$$

In a similar manner, we find the integrand which is proportional to $(\mathbf{r}_T' - \mathbf{r}_{T,i}) \ln(|\mathbf{r}_T' - \mathbf{r}_{T,i}|)$, in Eq. (3.33) while omitting the occurring constants

$$\begin{gathered}\iint_D (\mathbf{r}_T' - \mathbf{r}_{T,i}) \ln(|\mathbf{r}_T' - \mathbf{r}_{T,i}|) dA' = \\ \sum_{l=1}^{3} \frac{\mathbf{n}_l}{4} \Big\{ (d_{\max,l} - d_{\mathrm{col},il})^2 I_0(s_{a,l} - s_{\mathrm{col},il}, s_{b,l} - s_{\mathrm{col},il}; d_{\max,l} - d_{\mathrm{col},il}) \\ + I_2(s_{a,l} - s_{\mathrm{col},il}, s_{b,l} - s_{\mathrm{col},il}; d_{\max,l} - d_{\mathrm{col},il}) \Big\}. \end{gathered} \quad (3.37)$$

Substitution of Eqs. (3.34) and (3.37) in Eq. (3.33) results in an expression written in terms of standard integrals I_0 and I_2

$$\begin{gathered}\iint_D \ln(|\mathbf{r}_T' - \mathbf{r}_{T,i}|) E_y(\mathbf{r}_T') dA' = \\ \sum_{j=1}^{3} \sum_{l=1}^{3} \hat{E}_{y,j} \Big\{ M_{ijl} I_0(s_{a,l} - s_{\mathrm{col},il}, s_{b,l} - s_{\mathrm{col},il}; d_{\max,l} - d_{\mathrm{col},il}) \\ - N_{jl} I_2(s_{a,l} - s_{\mathrm{col},il}, s_{b,l} - s_{\mathrm{col},il}; d_{\max,l} - d_{\mathrm{col},il}) \Big\} \end{gathered} \quad (3.38)$$

where we have introduced the two matrices M and N as

$$\begin{aligned} M_{ijl} &= \left[1+\frac{\mathbf{n}_j\cdot(\mathbf{r}_{T,j}-\mathbf{r}_{T,i})}{d_{\text{max},j}}-\frac{\mathbf{n}_j\cdot\mathbf{n}_l}{d_{\text{max},j}}(d_{\text{max},l}-d_{\text{col},il})\right]\frac{(d_{\text{max},l}-d_{\text{col},il})}{4} && (3.39)\\ N_{jl} &= \frac{\mathbf{n}_j\cdot\mathbf{n}_l}{d_{\text{max},j}}. && (3.40)\end{aligned}$$

Now, the regular integral will be solved in a closed form, by applying the linear expansion functions for the electric field

$$\begin{aligned} I_{\text{reg}} &= \{\ln(2)-\varepsilon-\ln(\gamma)\}\iint_D E_y(\mathbf{r}_T')dA' \\ &= \{\ln(2)-\varepsilon-\ln(\gamma)\}\sum_{j=1}^{3}\hat{E}_{y,j}\iint_D f_j(\mathbf{r}_T'))dA' \\ &= \{\ln(2)-\varepsilon-\ln(\gamma)\}\frac{\text{Area}(D)}{3}\sum_{j=1}^{3}\hat{E}_{y,j} && (3.41)\end{aligned}$$

where Area(D) is the area of the triangular surface, D. Since γ may be a complex number, attention is required for the logarithm in Eq. (3.41) so that we write

$$\ln(\gamma)=\ln(-ik_0)=\ln(k_0)+\frac{\pi}{2}i. \tag{3.42}$$

Hence, the surface integral with regular kernel in Eq. (3.41) is

$$I_{\text{reg}}=\{\ln(2/k_0)-\varepsilon+\frac{\pi}{2}i\}\frac{\text{Area}(D)}{3}\sum_{j=1}^{3}\hat{E}_{y,j}. \tag{3.43}$$

Finally, using the expressions found for the integral with regular and singular kernel in Eqs. (3.41-3.38), the discretized electric field integral equation is found as

$$\begin{aligned}\hat{E}_y(\mathbf{r}_{T,i}) = \hat{E}_y^p(\mathbf{r}_{T,i}) + \frac{k_0^2\chi_e}{2\pi}\sum_{j=1}^{3}\hat{E}_{y,j}\Big\{\Big(\ln(2/k_0)-\varepsilon+\frac{\pi}{2}i\Big)\frac{\text{Area}(D)}{3} \\ -\sum_{l=1}^{3}M_{ijl}I_0(s_{A,l}-s_{\text{colil}},s_{B,l}-s_{\text{col},il};d_{\text{max},l}-d_{\text{col},il}) \\ +N_{jl}I_2(s_{A,l}-s_{\text{col},il},s_{B,l}-s_{\text{col},il};d_{\text{max},l}-d_{\text{col},il})\Big\} \qquad (3.44)\end{aligned}$$

where we have expressed the surface integrals in terms of standard line integrals and the constants (M, N) given in Eq. (3.39). As mentioned at the begin of this section, to solve the integral equation via the point matching method, an appropriate set of collocation points must be chosen.

For triangular basis functions, we have to solve a 3x3 matrix. The matrix counterpart of the electric field integral equation is found as

$$\left([K] - \tfrac{k_0^2\chi_e}{2\pi}\{[R]+[S]\} \right) \begin{pmatrix} \hat{E}_{y,1} \\ \hat{E}_{y,2} \\ \hat{E}_{y,3} \end{pmatrix} = \begin{pmatrix} \hat{E}^p_y(\mathbf{r}_{T,1}) \\ \hat{E}^p_y(\mathbf{r}_{T,2}) \\ \hat{E}^p_y(\mathbf{r}_{T,3}) \end{pmatrix} \tag{3.45}$$

with

$$[K] = f_j(\mathbf{r}_{T,i})[U] \qquad \text{and} \qquad [R] = \left(\ln(2/k_0) - \varepsilon + \frac{\pi}{2}i\right)\frac{\text{Area}(D)}{3}[U] \tag{3.46}$$

where $[U]$ is the unit matrix, i.e. the matrix with elements $U_{ij} = 1$. The 3×3 matrix elements resulting from the evaluation of the surface integral with singular kernel is found as

$$\begin{aligned} S_{ij} = -\sum_{l=1}^{3} \Big\{ & M_{ijl} I_0(s_{a,l} - s_{\text{col},il}, s_{b,l} - s_{\text{col},il}; d_{\max,l} - d_{\text{col},il}) \\ & + N_{jl} I_2(s_{a,l} - s_{\text{col},il}, s_{b,l} - s_{\text{col},il}; d_{\max,l} - d_{\text{col},il}) \Big\}. \end{aligned} \tag{3.47}$$

3.2 Electric Far-Field

Once the field amplitudes $\hat{E}_{y,j}$ are known, the scattered field at position $\mathbf{r}_T$ far away from the object can be easily evaluated from the integral representation

$$E^s_y(\mathbf{r}_T) = \frac{k_0^2}{2\pi}\chi_e \sum_{j=1}^{3} \hat{E}_{y,j} \iint_D K_0(-ik_0|\mathbf{r}_T - \mathbf{r}'_T|) f_j(\mathbf{r}'_T) dA. \tag{3.48}$$

In the far-field region, we may use a large-argument approximation for the modified Bessel function [9]

$$K_0(-i\rho) = \sqrt{\frac{\pi}{2\rho}}\exp(i\rho - i\pi/4) \qquad \text{for} \qquad \rho \gg 1 \tag{3.49}$$

where for the distance function $|\mathbf{r}_T - \mathbf{r}'_T|$, the approximation below is valid

$$|\mathbf{r}_T - \mathbf{r}'_T| \approx r_T - (\hat{\mathbf{r}}_T \cdot \mathbf{r}'_T) + O(\mathbf{r}_T^{-1}) \qquad \text{for} \qquad \mathbf{r}_T \gg \mathbf{r}'_T. \tag{3.50}$$

Substituting Eq. (3.49) and (3.50) in Eq. (3.48) results in the following expression for the scattered electric far-field

$$E^s_y(\mathbf{r}_T) = \Gamma_0(\mathbf{r}_T)\Phi(\theta) \tag{3.51}$$

where we identify Γ_0 as the equivalent line source

$$\Gamma_0(\mathbf{r}_T) = \frac{k_T^2}{\sqrt{8\pi k_0 r_T}}\exp(ik_0 r_T - i\pi/4) \tag{3.52}$$

and $\Phi(\theta)$ as the radiation pattern

$$\Phi(\theta) = -\chi_e \sum_{j=1}^{3} E_{y,j} \iint_D \exp(-i\mathbf{k}_T \cdot \mathbf{r}_T^{'}) f_j(\mathbf{r}_T^{'}) dA. \tag{3.53}$$

The two-dimensional integral over the domain D in Eq. (3.53) will be transformed into a integral over the boundary ∂D by using Green's second identity

$$\iint_D a\nabla_T^2 b - b\nabla_T^2 a dA = \oint_{\partial D} \{a\partial_n b - b\partial_n a\}\, dl \tag{3.54}$$

where a and b are scalar functions and ∂_n denotes the directional derivative along the outward pointing normal n with respect to boundary ∂D. The surface integral, as found in Eq. (3.53), will now be casted in the form of the left-hand side of Eq. (3.54)

$$\begin{aligned} -\frac{1}{k_0^2} \int_D \left\{ f_j(\mathbf{r}_T^{'}) \nabla_T^2 \exp(-i\mathbf{k}_T \cdot \mathbf{r}_T^{'}) - \exp(-i\mathbf{k}_T \cdot \mathbf{r}_T^{'}) \nabla_T^2 f_j(\mathbf{r}_T^{'}) \right\} dA' = \\ -\frac{1}{k_0^2} \oint_{\partial D} \left\{ f_j(\mathbf{r}_T^{'}) \partial_n \exp(-i\mathbf{k}_T \cdot \mathbf{r}_T^{'}) - \exp(-i\mathbf{k}_T \cdot \mathbf{r}_T^{'}) \partial_n f_j(\mathbf{r}_T^{'}) \right\} dl \end{aligned} \tag{3.55}$$

where $\nabla_T^2 f_j(\mathbf{r}_T^{'}) = 0$ as a consequence of the linear behavior of the basis functions. The two derivatives at the right-hand side of Eq. (3.55) can be written as

$$\partial_n \exp(-i\mathbf{k}_T \mathbf{r}_T) = (i\mathbf{k}_T \cdot \mathbf{n}) \exp(i\mathbf{k}_T \cdot \mathbf{r}_T) \tag{3.56}$$

$$\partial_n f_j(\mathbf{r}_T) = -\frac{\mathbf{n}_j \cdot \mathbf{n}}{d_{\max,j}}. \tag{3.57}$$

Next, we write the boundary integral in Eq (3.55) as a sum of line integrals. Therefore, we use the parameterization procedure as defined in Eq. (3.20), i.e. $\mathbf{r}_T = d\mathbf{n}_l + s\boldsymbol{\tau}_l$, where $\mathbf{n}_l$ and $\boldsymbol{\tau}_l$ are constant vectors with respect to a single line segment indicated by subscript, l. Substituting Eqs. (3.56-3.57) in Eq. (3.55) and using the defined parameterization yields

$$\begin{aligned} -\frac{1}{k_0^2} \oint_{\partial D} \left\{ f_j(\mathbf{r}_T^{'}) \partial_n \exp(-i\mathbf{k}_T) - \exp(-i\mathbf{k}_T) \partial_n f_j(\mathbf{r}_T^{'}) \right\} dl = \\ -\frac{1}{k_0^2} \sum_{l=1}^{3} \int_{s_{a,l}}^{s_{b,l}} \left[\left(1 + \frac{\mathbf{n}_j \cdot \mathbf{r}_{T,j} - \mathbf{n}_j \cdot \mathbf{n}_l d_{\max,l}}{d_{\max,j}} \right) (i\mathbf{k}_T \cdot \mathbf{n}_l) + \left(\frac{\mathbf{n}_j \cdot \mathbf{n}_l}{d_{\max,j}} \right) \right] + \\ \left[-(i\mathbf{k}_T \cdot \mathbf{n}_l) \frac{\mathbf{n}_j \cdot \boldsymbol{\tau}_i}{d_{\max,j}} \right] s \exp(i\mathbf{k}_T \cdot (d_l \mathbf{n}_l + s\boldsymbol{\tau}_l)) ds \end{aligned} \tag{3.58}$$

with d_l is constant at a single line segment and s vary between $s_{a,l}$ and $s_{b,l}$. In short-hand notation we write for the right-hand side of Eq. (3.58)

$$-\frac{1}{k_0^2} \sum_{l=1}^{3} \int_{s_{a,i}}^{s_{b,i}} [A_{lj} + B_{lj} s] \exp(C_l + D_l s) ds \tag{3.59}$$

where the constants are given by

$$\begin{aligned}
A_{lj} &= \left[\left(1+\frac{\mathbf{n}_j\cdot\mathbf{r}_{T,j}-\mathbf{n}_j\cdot\mathbf{n}_l d_{\max,l}}{d_{\max,j}}\right)(i\mathbf{k}_T\cdot\mathbf{n}_l)+\left(\frac{\mathbf{n}_j\cdot\mathbf{n}_l}{d_{\max,j}}\right)\right] && (3.60)\\
B_{lj} &= \left[-(i\mathbf{k}_T\cdot\mathbf{n}_l)\frac{\mathbf{n}_j\cdot\boldsymbol{\tau}_i}{d_{\max,j}}\right] && (3.61)\\
C_l &= i\mathbf{k}_T\cdot\mathbf{n}_l d_{\max,l} && (3.62)\\
D_l &= i\mathbf{k}_T\cdot\boldsymbol{\tau}_l. && (3.63)
\end{aligned}$$

We have now obtained the representation for the scattered electric far-field in a closed form. In Chapter 5 we will compare the electric field inside the object and the electric far-field computed with the in this chapter developed method with an alternative solution method. Numerical computations have demonstrated that for a large wavelength of the electric field inside the object the difference between the approximated electric far-field and the actual electric far-field is small.

In the next chapter, which is concerned with diffraction gratings, we will use the knowledge gained in this chapter with respect to the point matching method, the assumption of the wavelength of the electric field and the triangular basis functions and the surface integral to boundary integral transformation technique.

Chapter 4

Diffraction gratings

In this chapter we consider the scattering of an electrically polarized plane wave by a diffraction grating which is periodic in one dimension. The diffraction grating consists of a periodic structure placed on the planar interface between two half spaces with different electromagnetic properties. The assumption introduced in Chapter 3, namely that the wavelength of the electric field inside the object is much larger than the maximum dimension of the object ($L_{\text{max}} < 0.25\lambda_{\text{mat}}$) also applies for the next derivations. We formulate the scattering problem as a domain integral equation, where the appearing integrals over a 2D domain will be solved in a closed form. Finally, the aim is to find the reflection coefficients using a spectral and spatial domain approach.

4.1 Formulation of the problem

The diffraction grating under consideration is invariant in the y-direction and consist of a structure, periodic in the x-direction, placed on the planar interface between two half spaces. The transverse cross section of the diffraction grating is shown in Fig. 4.1. In the next considerations, the upper half space, i.e. $z \geq 0$, is free space thus the permittivity is given by $\epsilon_1 = \epsilon_0$. For the lower half space ($z < 0$) we use a medium which has a complex permittivity $\epsilon_2 = \epsilon_2' + i\epsilon_2''$. The structure embedded in the upper half space is made of a material with complex permittivity $\epsilon_{\text{mat}} = \epsilon_{\text{mat}}' + i\epsilon_{\text{mat}}''$. All media in the configuration are non-magnetic, therefore the permeabilities are $\mu_1 = \mu_2 = \mu_{\text{mat}} = \mu_0$. The length of one period of the structure is indicated by dimension a. We assume that the object has a trapezoidal transverse cross section.

The grating is illuminated by an electrically polarized plane wave which is aligned in the invariant y-direction of the configuration. The angle of incidence of the incident field lies in the transverse plane, such that we consider planar diffraction. Since the incident field is polarized in the y-direction and has no spatial dependence in the invariant direction of the configuration, the three-dimensional electromagnetic scattering problem reduces into a two-dimensional problem. The resulting electric field is then found as the solution of the two-dimensional Helmholtz equation in two half spaces with different material properties.

The formulation of the scattering problem is based on the decomposition of the total electric field in a primary electric field and a secondary electric field. We define the primary electric field

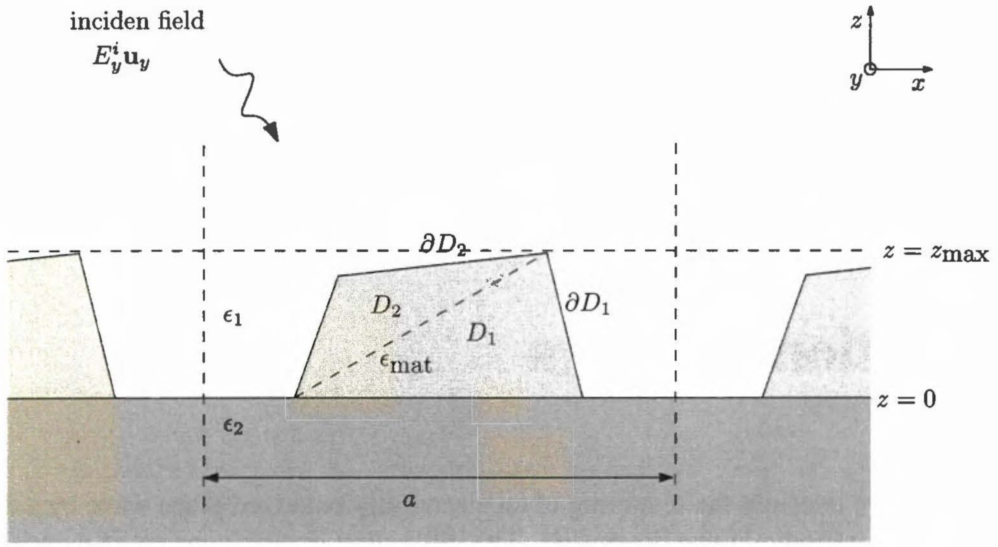

Figure 4.1: Transverse cross section of 1D diffraction grating.

as the electric field due to the polarized incident electric plane wave in the presence of two half spaces. The secondary electric field is defined as the field which results from the combined effects of a secondary current distribution caused by an impressed source or an inhomogeneity in the permittivity and of the two half spaces. These two field problems will be discussed successively where we start with the primary field problem.

4.2 Primary electric field

The incident field is defined as the electrically polarized unit-amplitude plane wave in free space with time dependence $\exp(-i\omega t)$

$$\mathbf{E}(\mathbf{r}_T) = \exp(ik^i_{0x}x - ik^i_{0z}z)\mathbf{u}_y \tag{4.1}$$

where $k^i_{0x} = k_0 \cos(\theta_i)$ and $k^i_{0z} = k_0 \sin(\theta_i)$ with θ_i the angle of incidence lying in the transverse plane (x, z). The free-space wave number is defined as $k_0 = \omega\sqrt{\mu_0\epsilon_0}$. The inclusion of two half spaces leads to the following expression for the primary electric field in the upper half space

$$E^p_y(x, z) = \exp(ik^i_{0x}x - ik^i_{0z}z) + R^{\text{prim}} \exp(ik^i_{0x}x + ik^i_{0z}z) \quad \text{for} \quad z \geq 0 \tag{4.2}$$

where the superscript ^{p} refers to the primary electric field. The reflection coefficient R^{prim} resulting from the reflection of the lower half space is found as

$$R^{\text{prim}} = \frac{\sqrt{\epsilon_1}\cos(\theta_i) - \sqrt{\epsilon_2 - \epsilon_1\cos^2(\theta_i)}}{\sqrt{\epsilon_1}\cos(\theta_i) + \sqrt{\epsilon_2 - \epsilon_1\cos^2(\theta_i)}} \tag{4.3}$$

For the evaluation of the square root of the complex permittivity ϵ_2 in Eq. (4.2-4.3) special attention is required. The choice of the square root is determined by the requirement that the total electric field should remain bounded and/or representing outgoing propagating waves when $|z| \to \infty$. Since the primary electric field in Eq. (4.2) is bounded and represents propagating waves, the choice of the square root is determined by the radiation condition applied to the primary electric field in the lower half space, i.e. for $z < 0$. The electric field in the lower half space is found as

$$E_y^p(x,z) = T^{\mathrm{prim}} \exp(ik_{2x}x - i\mathbf{k}_{2z}z) \qquad \text{for} \quad z < 0 \tag{4.4}$$

where $T^{\mathrm{prim}} = 1 + R^{\mathrm{prim}}$ is the transmission coefficient and $k_{2x} = k_{0x}^i$. The wave number $\mathbf{k}_{2z}$ in Eq.(4.4) is now a complex number as a consequence of the complex permittivity in the lower half space. Applying the boundary conditions to the electric field in the upper half space and the lower half space leads to the determination of the complex wave number

$$\mathbf{k}_{2z} = \sqrt{(\epsilon_2' + i\epsilon_2'')k_0^2 - (k_{0x}^i)^2} = \mathrm{Re}(k_{2z}) + i\mathrm{Im}(k_{2z}). \tag{4.5}$$

Substitution of Eq. (4.5) in Eq. (4.4) shows that the primary electric field in the lower half space is only bounded and represents propagating waves when $\mathrm{Re}(k_{2z}) > 0$ or $\mathrm{Re}(k_{2z}) = 0$ and $\mathrm{Im}(k_{2z}) > 0$ for $z \to -\infty$. This means that the principal value of the square root of the complex permittivity leads to the conditions

$$\mathrm{Re}(\sqrt{\epsilon_2}) > 0 \qquad \text{or} \qquad \mathrm{Re}(\sqrt{\epsilon_2}) = 0 \quad \text{and} \quad \mathrm{Im}(\sqrt{\epsilon_2}) > 0. \tag{4.6}$$

4.3 Secondary electric field

4.3.1 Homogeneous space

We start to formulate the scattered field in a homogeneous space with constant complex permittivity ϵ in terms of a general electric current distribution $\mathbf{J}$. The current distribution $\mathbf{J}$ originates from an impressed source or an inhomogeneity in the permittivity enclosed by ∂D and is depicted in Fig. 4.2(a). The general solution for the electric field can be found from Maxwell equation's in the frequency domain

$$\begin{aligned} \nabla \times \mathbf{H}^s &= \mathbf{J} - i\omega\epsilon\mathbf{E}^s && (4.7) \\ \nabla \times \mathbf{E}^s &= i\omega\mu_0\mathbf{H}^s && (4.8) \end{aligned}$$

where the field quantities with superscript ^{s} denote the scattered fields. When we take the curl of Eq. (4.8) and combine Eq. (4.7) and (4.8) we find that

$$\nabla \times \nabla \times \mathbf{E}^s = i\omega\mu_0\mathbf{J} + i\omega^2\epsilon\mu_0\mathbf{E}^s. \tag{4.9}$$

The left-hand side can be written as

$$\nabla \times \nabla \times \mathbf{E}^s = \nabla(\nabla \cdot \mathbf{E}^s) - \nabla^2\mathbf{E}^s. \tag{4.10}$$

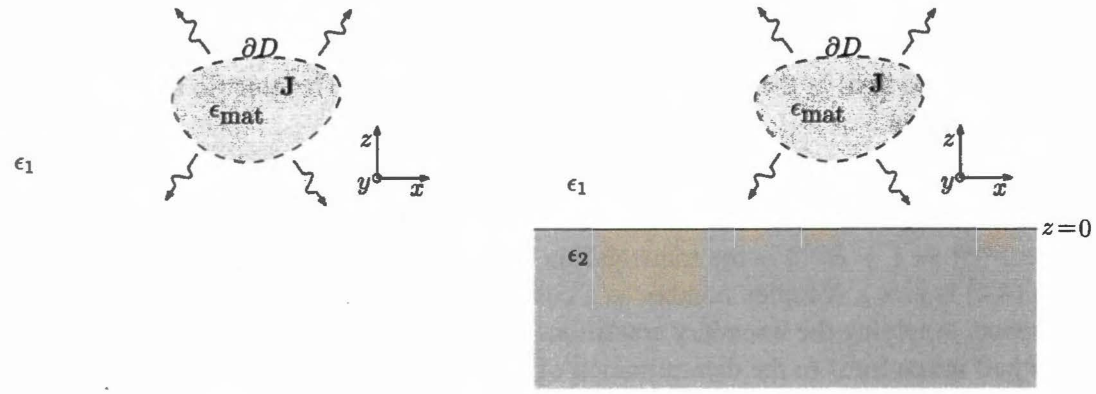

(a) (b)

Figure 4.2: Transverse cross section of object (a) in homogeneous space (b) in two half spaces.

Since we consider the special case where $\mathbf{E} = E_y(x,z)\mathbf{u}_y$, the divergence term on the right-hand side of Eq. (4.10) can be rewritten as

$$\nabla \cdot \mathbf{E}^s = \partial_y E_y^s \tag{4.11}$$

so that Eq. (4.9) results in

$$\left(\nabla_T^2 + \frac{\omega^2}{c_0^2}\epsilon_r\right) E_y^s(x,z) = -i\omega\mu_0 J_y(x,z). \tag{4.12}$$

where the relative permittivity is given by $\epsilon_r = \epsilon/\epsilon_0$.

Since we will include the effects of a half space composed of two media, where $\epsilon(z)$ depends only in z, we may introduce a single spatial transformation over the remaining spatial variable, i.e. x, so that the second-order differential equation can be reduced to a sequence of one-dimensional differential equations. The spatial Fourier transform pair is given by

$$\hat{E}_y(k_x,z) = \int_{-\infty}^{\infty} \exp(-ik_x x) E_y(x,z)dx \tag{4.13}$$

$$E_y(x,z) = \frac{1}{2\pi}\int_{-\infty}^{\infty} \exp(ik_x x)\hat{E}_y(k_x,z)dk_x \tag{4.14}$$

which is in accordance with the temporal Fourier transform pair. By applying Eq. (4.13) to Eq. (4.12), the following one-dimensional wave equation results

$$\partial_z^2 \hat{E}_y^s + (\frac{\omega^2}{c_0^2}\epsilon_r - k_x^2)\hat{E}_y^s = -i\omega\mu_0\hat{J}_y. \tag{4.15}$$

In the case of one homogeneous space with relative complex permittivity ϵ_r, we define Green's function as the solution of

$$\partial_z^2 G_1 - \gamma_1^2 G_1 = -\delta(z - z') \quad \text{for} \quad z \in \mathbb{R} \tag{4.16}$$

where $\gamma_1 = \sqrt{k_x^2 - \frac{\omega^2}{c_0^2}\epsilon_{r1}}$ and δ is a Dirac delta distribution representing a point source located at z'. In the most general form, the solution of Eq. (4.16) is found as

$$G_1 = \frac{1}{2\gamma_1}\exp(-\gamma_1|z-z'|) + P\exp(\gamma_1 z) + Q\exp(-\gamma_1 z) \tag{4.17}$$

which in addition should remain bounded or representing outgoing waves when $|z| \to \infty$. The requirement that Green's function must satisfy the radiation condition implies that $P = Q = 0$ and results in the solution of Eq. (4.16)

$$G_1 = \frac{1}{2\gamma_1}\exp(-\gamma_1|z-z'|) \tag{4.18}$$

where the appearance of the square root of γ_1 results in the choice of the branch cut to be $\mathrm{Re}(\gamma_1) \geq 0$ and $\mathrm{Im}(\gamma_1) < 0$ which is in accordance with the radiation condition for a homogeneous space with complex permittivity.

Owing to the superposition principle, the solution of Eq. (4.15) can be easily generalized from the results of Eq. (4.17), i.e.

$$\hat{E}_y^s = i\omega\mu_0 \int_{-\infty}^{\infty} G_1(z,z')\hat{J}_y(k_x,z')dz' \tag{4.19}$$

which expresses $\hat{E}_y$ in terms of the spatial Fourier transform of $\hat{J}_y(k_x, z)$.

4.3.2 Half space

Next, we include the effects of two half spaces. The upper half space ($z \geq 0$) consist of free space ($\epsilon_1 = \epsilon_0$) and the lower half space ($z < 0$) is made a medium with a complex permittivity ϵ_2. The configuration is shown in Figure 4.2(b). For the two half spaces Eq. (4.16) changes to

$$\begin{aligned} \partial_z^2 G - \gamma_1^2 G &= -\delta(z-z') && \text{for} \quad z \geq 0 \\ \partial_z^2 G - \gamma_2^2 G &= 0 && \text{for} \quad z < 0. \end{aligned} \tag{4.20}$$

The general solution of Eq. (4.20) can be written as

$$G = \begin{cases} G_1(z,z') + A\exp(-\gamma_1 z) & \text{for} \quad z \geq 0 \\ B\exp(\gamma_2 z) & \text{for} \quad z < 0 \end{cases} \tag{4.21}$$

where $\gamma_i = \sqrt{k_x^2 - k_0^2\epsilon_{r,i}}$ with $i \in (1,2)$. The requirement that G must satisfy the radiation condition leads to the choice of the square root of γ_i. The upper half space consist of free space so that γ_1^2 is real (positive and negative) which means that $\mathrm{Re}(\gamma_1) > 0$ or $\mathrm{Re}(\gamma_1) = 0$ and $\mathrm{Im}(\gamma_1) < 0$. The lower half space has a material property with complex permitivity so that the radiation condition is fulfilled when $\mathrm{Re}(\gamma_2) \geq 0$ and $\mathrm{Im}(\gamma_2) < 0$.

The coefficients in Eq. (4.21) are found from the boundary conditions at the interface between the two media at $z = 0$. It follows that E_y and H_x are continuous and consequently G and $\partial_z G$ thus it means that Eq. (4.21) can be written as

$$\begin{aligned} \frac{1}{2\gamma_1}\exp(-\gamma_1 z') + A &= B && (4.22) \\ \frac{1}{2}\exp(-\gamma_1 z') - \gamma_1 A &= \gamma_2 B && (4.23) \end{aligned}$$

with the solution

$$\begin{aligned} A &= \frac{1}{2\gamma_1}\exp(-\gamma_1 z')\frac{\gamma_1 - \gamma_2}{\gamma_1 + \gamma_2} && (4.24) \\ B &= \frac{1}{2\gamma_1}\frac{2\gamma_1}{\gamma_1 + \gamma_2}\exp(-\gamma_1 z') && (4.25) \end{aligned}$$

where the Fresnel reflection and transmission coefficient are recognized as

$$\begin{aligned} \bar{R} &= \frac{\gamma_1 - \gamma_2}{\gamma_1 + \gamma_2} && (4.26) \\ \bar{T} &= \frac{2\gamma_1}{\gamma_1 + \gamma_2}. && (4.27) \end{aligned}$$

It means that the final expression for Green's function G can be written as

$$G = \begin{cases} \frac{1}{2\gamma_1}[\exp(-\gamma_1|z - z'|) + R\exp(-\gamma_1 z' - \gamma_1 z)] & \text{for} \quad z \geq 0 \\ \frac{1}{2\gamma_2} T\exp(-\gamma_2 z' + \gamma_1 z) & \text{for} \quad z < 0. \end{cases} \qquad (4.28)$$

Because we are only interested in the (far-) field in the upper half space we combine Eq. (4.14), (4.19) and (4.28) to find a spectral representation for the (far-) field at $z > 0$

$$\begin{aligned} E_y^s(x, z) &= \frac{i\omega\mu_0}{2\pi}\int_{-\infty}^{\infty}\frac{dk_x}{2\gamma_1}\exp(ik_x x)\int_0^{z_{\max}}\exp(-\gamma_1|z - z'|)\hat{J}_y(k_x, z')dz' \\ &+ \frac{i\omega\mu_0}{2\pi}\int_{-\infty}^{\infty}\frac{dk_x}{2\gamma_1}R\exp(ik_x x - \gamma_1 z)\int_0^{z_{\max}}\exp(-\gamma_1 z')\hat{J}_y(k_x, z')dz', \quad (4.29) \end{aligned}$$

which is the expression that would have to be evaluated for a source distribution or an inhomogeneity at $z > 0$.

4.3.3 Periodicity

Next, we specify our configuration to a source distribution or an inhomogeneity which is periodic along the x-coordinate. Since we consider a medium which is periodic, the current distribution and the corresponding electric field are also periodic, so that we write for the current distribution [11]

$$J_y^s(x + a, z) = \exp(ik_{0x}^i x)j(x, z) \qquad (4.30)$$

with $j(x + na, z) = j(x, z)$ for $n = (0, \pm 1, \pm 2, \dots)$. The formulation used in Eq. (4.30) is known as Floquet's theorem which is a special case of Bloch's theorem, valid for three-dimensional periodicity. In Appendix B, we prove Bloch's theorem for macroscopic electromagnetic fields.

For the periodic function $j(x, z)$, an infinite series of orthonormal expansion functions also known as the discrete Fourier transform are used [12]

$$j(x, z) = \sum_{n=-\infty}^{\infty} j_n(z) \exp(i\frac{2\pi}{a}nx) \tag{4.31}$$

where the Fourier coefficients $j_n(z)$ are given by

$$j_n(z) = \frac{1}{a}\int_0^a \exp(-i\frac{2\pi}{a}nx) j(x, z) dx. \tag{4.32}$$

Substituting Eq. (4.30) in (4.32) yields

$$j_n(z) = \frac{1}{a}\int_0^a \exp(-ik_x^i x - i\frac{2\pi}{a}nx) J_y^s(x, z) dx \tag{4.33}$$

i.e. the one-dimensional Fourier transform of $J_y^s(x, z)$ at $k_{xn} = k_{0x}^i + n\frac{2\pi}{a}$.
Comparison of Eq. (4.33) with Eqs. (4.13)-(4.14) shows that the integration is only evaluated over one period and the factors a and 2π occur at different positions.

In order to use Eq. (4.29) we transform Eq. (4.31) by means of a spatial Fourier transform over variable x which result in a discrete series, i.e.

$$\hat{J}_y(k_x, z) = 2\pi \sum_{n=-\infty}^{\infty} j_n(z) \delta(k_x - k_x^i - n\frac{2\pi}{a}). \tag{4.34}$$

When substituting Eq. (4.34) in Eq. (4.29), we obtain the final expression for the scattered electric field in $z > 0$

$$\begin{aligned} E_y^s(x, z) &= i\omega\mu_0 \sum_{n=-\infty}^{\infty} \frac{\exp(ik_{xn}x)}{2\gamma_{1n}} \int_0^{z_{max}} \exp(-\gamma_{1n}|z - z'|) j_n(z') dz' \\ &+ i\omega\mu_0 \sum_{n=-\infty}^{\infty} \frac{\bar{R}_n \exp(ik_{xn}x - \gamma_{1n}z)}{2\gamma_{1n}} \int_0^{z_{max}} \exp(-\gamma_{1n}z') j_n(z') dz' \end{aligned} \tag{4.35}$$

which gives the scattered electric field in terms of a series of Fourier integrals of $J_y^s(x, z)$ where $\gamma_{i,n}$ and $\bar{R}_n$ depends on the spectral order n as a result of k_{xn}.

When considering the last integral in Eq. (4.35) in more detail and using the results of Eq. (4.34) we find that

$$\int_0^{z_{max}} \exp(-\gamma_{1n}z') j_n(z') dz' = \frac{1}{a}\int_0^a dx' \int_0^{z_{max}} \exp(-ik_{xn}x - \gamma_{1n}z) J_y^s(x', z') dz' \tag{4.36}$$

which is in fact a normalized modified spatial Fourier transform. A similar expression can now be derived in the same manner for the first integral, i.e.

$$\begin{aligned}\int_0^{z_{max}} \exp(-\gamma_{1n}|z-z'|)j_n(z')dz' = \\ \frac{\exp(-\gamma_{1n}z)}{a}\int_0^a dx' \int_0^z \exp(-ik_{xn}x' + \gamma_{1n}z')J_y^s(x',z')dz' \\ + \frac{\exp(\gamma_{1n}z)}{a}\int_0^a dx' \int_z^{z_{max}} \exp(-ik_{xn}x' - \gamma_{1n}z')J_y^s(x',z')dz' \quad (4.37)\end{aligned}$$

where a linear combination of two spatial Fourier transforms are used to account for observation positions between $z = 0$ and $z = z_{max}$. This means that the surface integral over domain D splits into a sum of integrals over two subdomains. As shown at the right-hand side of Eq. (4.37), the two spatial Fourier transforms differ only in the sign in the exponent but have a similar form. Therefore, knowing that the first spatial integral can be found by replacing γ_1 by $-\gamma_1$ we rewrite the second spatial integral in Eq. (4.37) in terms of line integrals. For that purpose we use Green's second identity

$$\begin{aligned}\frac{1}{a}\int_0^a dx' \int_0^z \exp(-ik_{xn}x - \gamma_{1n}z')J_y^s(x',z')dz' = \\ \frac{1}{(\gamma_{1n}^2 - k_{xn}^2)a}\int_D \left\{J_y^s(x',z')\nabla_T^2 \exp(-ik_{xn}x - \gamma_{1n}z')\right. \\ \left. - \exp(-ik_{xn}x - \gamma_{1n}z')\nabla_T^2 J_y^s(x',z')\right\} dx'dz' \\ = \frac{1}{-k_0^2\epsilon_{r1}a}\oint_{\partial D} \left\{J_y^s(x',z')\partial_n \exp(-ik_{xn}x - \gamma_{1n}z')\right. \\ \left. - \exp(-ik_{xn}x - \gamma_{1n}z')\partial_n J_y^s(x',z')\right\} dl' \quad (4.38)\end{aligned}$$

where ∂D is the boundary which encloses the trapezoidal shaped cross section of the object. We have also used that $\gamma_{1n}^2 - k_{xn}^2 = -\frac{\omega^2}{c_0}\epsilon_{r1} = -k_0^2\epsilon_{r1}$.

In analogy with the formulation for the electric field used in Chapter 3, we write the current density J_y^s in terms of the total electric field

$$J_y^s(x,z) = -i\omega(\epsilon_{\text{mat}} - \epsilon_1)E_y(x,z) \quad (4.39)$$

where ϵ_{mat} is the permitivitty of the material in domain ∂D and ϵ_1 is the permitivitty of the background medium, in this case free space with $\epsilon_1 = \epsilon_0$.

Since we have assumed that the wavelength of the electric field inside the object is large compared to the maximum dimensions of the object we use for the electric field a weighted sum of linear expansion functions

$$E_y(x,z) = \sum_{j=1}^{3} \hat{E}_{y,j}(x,z)f_j(x,z) \quad (4.40)$$

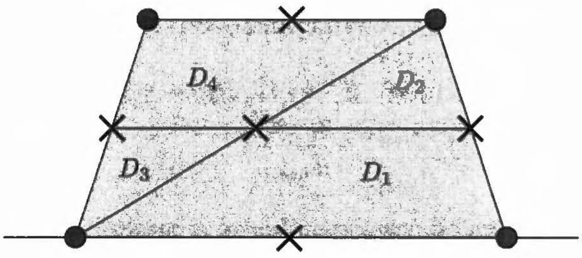

Figure 4.3: Definition of subdomains for trapezoidal cross section of object.

where the expansion function f_j is defined in Section 3.1.1 and $\hat{E}_{y,j}$ denotes the field amplitudes in the vertex positions of the object.

To approximate the electric field in the trapezoidal domain we realize this by defining two adjacent triangular domains with two sets of basis functions because the support of the expansion functions in Eq. (4.40) are defined inside a triangular domain. For the case that observation positions are chosen at the vertex positions the spatial Fourier transforms in Eq. (4.36) and (4.37) are evaluated over two triangular subdomains. For observation positions between $z = 0$ and $z = z_{\text{max}}$ the spatial Fourier transform in Eq. (4.37) leads to four subdomains. The decomposition of the trapezoidal domain is shown in Fig. 4.3.

As an example we will proceed with the evaluation of the spatial Fourier transform in Eq. (4.38) for subdomain D_1 since the contribution of the other subdomains to the scattered electric field can be evaluated in a similar manner.

The subdomain D_1 is delimited by four straight line segments. Substituting Eq. (4.39-4.40) in (4.38) then results in

$$\begin{aligned}&\frac{-i\omega(\epsilon_{\text{mat}}-\epsilon_1)}{a}\iint_{D_1}\exp(-ik_{xn}x-\gamma_{1n}z'))E_y(x',z')dx'dz' = \\ &\qquad\frac{i\omega(\epsilon_{\text{mat}}-\epsilon_1)}{k_0^2\epsilon_{r1}a}\sum_{j=1}^{3}\hat{E}_{y,j}\oint_{\partial D_1}\{f_j(x',z')\partial_n\exp(-ik_{xn}x'-\gamma_{1n}z') \\ &\qquad\qquad - \exp(-ik_{xn}x'-\gamma_{1n}z')\partial_n f_j(x',z')\}\,dl'.\end{aligned} \tag{4.41}$$

The resulting boundary integral on the right-hand side in Eq. (4.41), will be divided into four line integrals along the piecewise constant line segments that delimitates domain D_1. Further, the individual line integrals are rewritten into a local coordinate system, where at each line the tangent and the normal vectors are constant. To make use of these constant vectors the position vector along a straight line segment is defined as follows

$$\mathbf{r}_T = d\mathbf{n} + s\boldsymbol{\tau} \tag{4.42}$$

where d is constant and s the integration variable, analog to the parameterization procedure defined in Section 3.1.2.

Using this parameterization, the two directional derivatives in Eq. (4.41) can be written as

$$\begin{aligned}\partial_{nl}\exp(-ik_{xn}x' - \gamma_{1n}z') &= \mathbf{n}_l \cdot (-ik_{xn}\mathbf{u}_x - \gamma_{1n}\mathbf{u}_z)\exp(-ik_{xn}x' - \gamma_{1n}z') &(4.43)\\ \partial_{nl}f_j &= -\frac{\mathbf{n}_l \cdot \mathbf{n}_j}{d_{\mathrm{max},j}} &(4.44)\end{aligned}$$

where the derivatives are evaluated corresponding to a particular straight line segment indicated by the subscript, l. In similar manner, the spatial variables x' and z' are transformed in local coordinates

$$\begin{aligned}x' &= \mathbf{u}_x \cdot \mathbf{r}_{T,l} = \mathbf{u}_x \cdot (d_{\mathrm{max},l}\mathbf{n}_l + s\boldsymbol{\tau}_l) &(4.45)\\ z' &= \mathbf{u}_z \cdot \mathbf{r}_{T,l} = \mathbf{u}_z \cdot (d_{\mathrm{max},l}\mathbf{n}_l + s\boldsymbol{\tau}_l) &(4.46)\end{aligned}$$

valid for straight line segment l. Substituting Eq. (4.43-4.46) in the right-hand side of Eq. (4.41), and omitting the constant in front of the integral, we find

$$\sum_{j=1}^{3}\hat{E}_{y,j}\oint_{\partial D_1} f_j(x',z')\partial_n \exp(-ik_{xn}x' - \gamma_{1n}z') - \exp(-ik_{xn}x' + \gamma_{1n}z')\partial_n f_j(x',z')dl' =$$
$$\sum_{j=1}^{3}\sum_{l=1}^{4}\hat{E}_{y,j}\exp(D_l^n)\left[A_{l,j}^n \mathrm{L}_0(s_{a,l},s_{b,l},C_l^n) + B_{l,j}^n \mathrm{L}_1(s_{a,l},s_{b,l},C_l^n)\right] \qquad (4.47)$$

where we have defined the standard integral L_0 and L_1 as

$$\mathrm{L}_\alpha(s_{a,l},s_{b,l},\beta) = \int_{s_{a,l}}^{s_{b,l}} s^\alpha \exp(\beta s)ds \qquad (4.48)$$

where $s_{a,l}$ and $s_{b,l}$ denote the begin and end positions on the line segment l, respectively. The constants A, B, C and D are found as

$$\begin{aligned}A_{l,j}^n &= \left[1 + \frac{\mathbf{n}_j \cdot \mathbf{r}_{T,j} - d_{\mathrm{max},l}\mathbf{n}_l \cdot \mathbf{n}_j}{d_{\mathrm{max},j}}\right] \cdot (\mathbf{n}_l \cdot (-ik_{xn}\mathbf{u}_x - \gamma_n\mathbf{u}_z)) + \frac{\mathbf{n}_l \cdot \mathbf{n}_j}{d_{\mathrm{max},j}} &(4.49)\\ B_{l,j}^n &= \left(\frac{\mathbf{n}_j \cdot \boldsymbol{\tau}_l}{d_{\mathrm{max},j}}\right)(ik_{xn}(\mathbf{u}_x \cdot \mathbf{n}_l) + \gamma_n(\mathbf{n}_l \cdot \mathbf{u}_z)) &(4.50)\\ C_l^n &= -\left(ik_{xn}(\mathbf{u}_x \cdot \boldsymbol{\tau}_l) + \gamma_n(\mathbf{u}_z \cdot \boldsymbol{\tau}_l)\right) &(4.51)\\ D_l^n &= -\left(ik_{xn}d_{\mathrm{max},l}(\mathbf{u}_x \cdot \mathbf{n}_l) + \gamma_n d_{\mathrm{max},l}(\mathbf{u}_z \cdot \mathbf{n}_l)\right). &(4.52)\end{aligned}$$

A similar procedure can be applied to find the other spatial Fourier transform for the remaining subdomains. Once these contributions are known, the total electric field is found as the sum of the primary electric field and the secondary electric field.

For the discussed configuration, the total electric field is expanded in 6 linear basis functions inside the two subdomains. To find the fundamental unknowns corresponding to the basis functions, i.e. the electric field amplitudes at the vertex positions $\hat{E}_{y,j}$, we apply the point-matching method in a similar manner as discussed in Section 3.1.3 so that we have to choose test functions and collocation points to obtain a system of linear equations. In Fig. 4.3 we have indicated by the cross and the dot two sets of collocation points. The number of collocation points is equal to the number of basis functions, so by applying the point matching method we obtain a system of 6 equations with 6 unknowns characterized by a 6x6 matrix where the 6 field amplitudes $\hat{E}_{y,j}$ can be found by solving the system of equations. Once the fundamental unknowns are found, the secondary electric field in $z > 0$ results from reusing Eq. (4.35).

4.4 Reflection coefficients

As mentioned in the introduction of the thesis, when a diffraction grating is illuminated by an electromagnetic plane wave a discrete number of reflected waves results. The total electric field may therefore be written in terms of Floquet waves

$$E_y(x,z) = \sum_{n=-\infty}^{\infty} R_n^{\text{tot}} \exp(ik_{xn}x - \gamma_{1n}z) + E_y^i(x,z) \qquad 0 \le z \le \infty \tag{4.53}$$

where the reflection coefficient R_n^{tot} and the phase $\exp(ik_{xn}x - \gamma_{1n}z)$ depends on the shape of the diffraction grating.

In this chapter we have decomposed the scattered electric field into a primary electric field and a secondary field so that therefore we rewrite Eq. (4.53) in the following form

$$E_y(x,z) = \sum_{n=-\infty}^{\infty} R_n^{\text{sec}} \exp(ik_{xn}x - \gamma_{1n}z) + E_y^p(x,z) \qquad 0 \le z \le \infty \tag{4.54}$$

where the reflection coefficient at $(x,z) = (0,0)$ corresponding to the primary electric field is easily found as R^{prim} and is defined in Eq. (4.3). The reflection coefficient R_n^{sec} at $(x,z) = (0,0)$ corresponding to the secondary field is given by

$$\begin{aligned} R_n^{\text{sec}} = i\omega\mu_0 \frac{1}{2\gamma_{1n}} \Bigg[& \int_0^{z_{\text{max}}} \exp(\gamma_{1n}z') j_n(z') dz' \\ & + \bar{R}_n \int_0^{z_{\text{max}}} \exp(-\gamma_{1n}z') j_n(z') dz' \Bigg] . \end{aligned} \tag{4.55}$$

The total reflection coefficient at $(x,z) = (0, z_{\text{max}})$ can be written as

$$R_n^{\text{tot}} = R_n^{\text{sec}} \exp(-2\gamma_{1n}z_{\text{max}}) \qquad \text{for} \quad n \neq 0 \tag{4.56}$$

$$R_0^{\text{tot}} = (R^{\text{prim}} + R_0^{\text{sec}}) \exp(-2\gamma_{1n}z_{\text{max}}) \qquad \text{for} \quad n = 0 \tag{4.57}$$

where the additional phase factor $\exp(-2\gamma_{1n}z_{\text{max}})$ is due to the choice of the position of the reference plane from which where the reflection coefficients are defined. Once the reflection coefficients of the reflected waves and the phase are known the electric far field is fully specified by Eq. (4.53).

In Chapter 5 we will use the reflection coefficients to derive an expression for a related quantity, namely the diffraction efficiency. The diffraction efficiency gives a relation between the power of the reflected electromagnetic field in the different directions relative to a surface parallel to the mean plane of the grating and the power of the incident field. The diffraction efficiencies computed with the developed methods in this chapter will be compared with the diffraction efficiencies computed with the Rigorous-Coupled-Wave Approach (RCWA). For large wavelengths of the electric field inside the periodic structure accurate values of the diffraction efficiencies are found.

Chapter 5

Numerical Results

In this chapter, we validate the developed methods to compute the scattered electric field for a dielectric cylinder with a triangular and a trapezoidal cross section, embedded in free space and for a diffraction grating. Therefore, we will use alternative solution methods to compare the electric field computed with the developed methods, where we vary the wavelength of the incident electric field, the geometrical parameters and the material properties of the object. Finally, we will demonstrate the possibility to retrieve some geometrical parameters of the dielectric cylinder and of the diffraction grating.

5.1 Non-periodic dielectric cylinder

5.1.1 Reference program

To compare the electric field calculated with our method with an existing method, we use a in-house developed program [13] as reference. In this section, we refer further to the electric field calculated with this program as the reference or the measured field. This program computes the scattered electric field (both near-field and far-field) for a given object illuminated by an electrically polarized incident field. The electric field problem for the reference method is formulated in terms of a domain integral equation. The integral equation is numerically solved by the "marching-on-in-angle" method which facilitates the frequency-domain computations. The domain of interest is discretized using a fixed mesh size. The object is enclosed by a rectangular domain $(x, z) \in [-1, 1]$ which have $N_x \times N_z$ subregions. The convolution type structure of the continuous integral equation is preserved with this discretization procedure so that the integral equation can be solved with the aid of a repeated evaluation of the "conjugate-gradient FFT" method. From now on, we solve the electric field in the reference method with a grid consisting of 65×65 rectangular subregions. This leads to small mesh sizes and an accurate approximated electric field which resembles very closely the exact field.

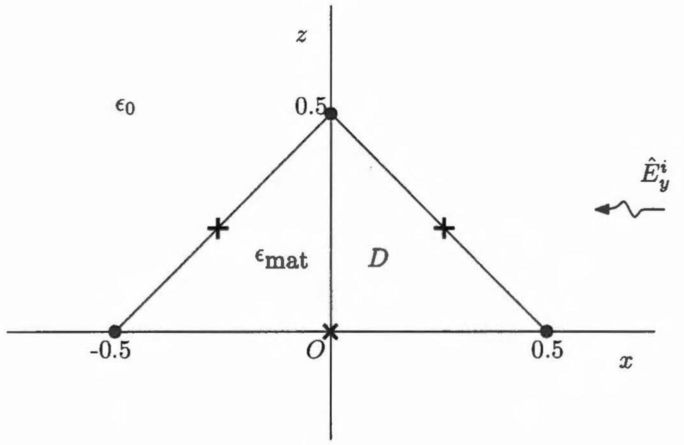

Figure 5.1: Transverse cross section of dielectric cylinder embedded in free space.

5.1.2 Electric field in object

We start to validate the developed method, discussed in Chapter 3, for the scattered electric field for an infinity long dielectric cylinder with a triangular cross section embedded in free space. The incident field is an electrically polarized plane wave, $\hat{E}^i_y \mathbf{n}_y$, which propagate in the $-x$-direction. The object is made of a homogeneous dielectric with refractive index $n_{\text{mat}} = \sqrt{\epsilon_{\text{mat}}} = 1.51$ where the embedding is free space. The structure under consideration is visualized in Fig. 5.1. We consider the shape of this object as the most general form since other triangular shapes will lead to similar results and other more complicated shapes can be constructed from the combination of triangular objects. The used solution method was based on the assumption that the wavelength of the electric field inside the object λ_{mat} is large compared to the maximum dimension of the object. Under this assumption the electric field inside the object can be approximated by linear basis functions. The wavelength inside the object is related to the fixed maximum dimension of the object denominated by the parameter L_{max}. The wavelength inside the object λ_{mat} is varied according to $4L_{\text{max}} \leq \lambda_{\text{mat}} \leq 20L_{\text{max}}$.

To find the electric field inside the object the integral equation should be solved. This is done via the point matching method, discussed in Chapter 3. Therefore, we have to choose an appropriate set of collocation points. We choose two sets of collocation points. The first set of points are the vertex points indicated by the dots (•) in Fig. 5.1. The second set is chosen at the centers of the edges between the two vertex points and is indicated by the cross (×) in Fig. 5.1.

To evaluate the influence of the collocation points on the value of the electric field, we will compute the electric field at the positions where the collocation points are taken with our approximated method. The electric field corresponding to these two cases are compared with the reference electric field at the collocation points. To that end, we define the relative error in the electric field at observation position $\mathbf{r}_T$ as

$$\sigma(\mathbf{r}_T) = \frac{|E^{\text{ref}}_y(\mathbf{r}_T) - E^{\text{approx}}_y(\mathbf{r}_T)|}{|E^{\text{ref}}_y(\mathbf{r}_T)|} \times 100\% \qquad (5.1)$$

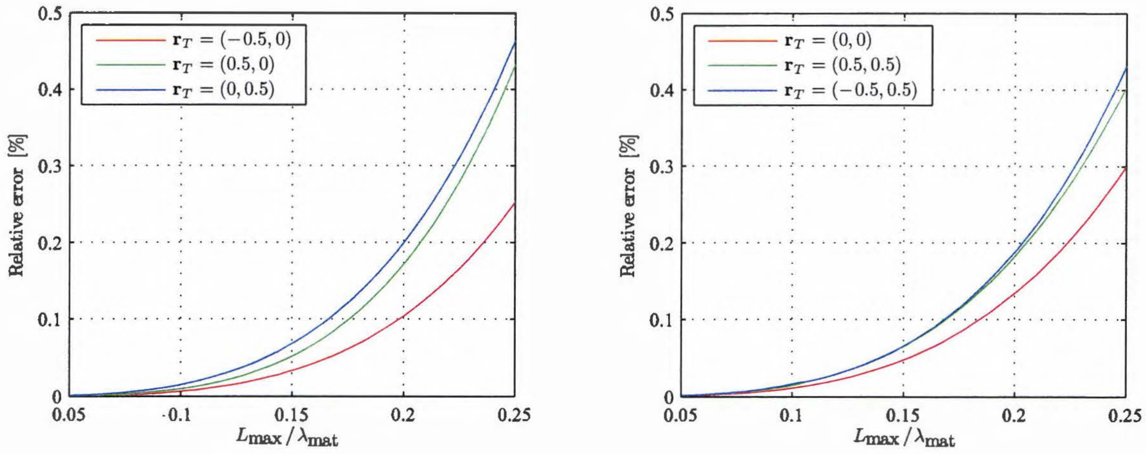

(a) (b)

Figure 5.2: Relative error [%] at the observation positions chosen at (a) the vertices and (b) at the centers of the edges for a dielectric object with refractive index $n = 1.51$.

where the reference electric field is indicated by $^{\mathrm{ref}}$ and our approximated electric field by $^{\mathrm{approx}}$. The relative error in the electric field calculated at the vertex points and at the center points are shown in Fig. 5.2(a) and 5.2(b), respectively as function of the maximum dimension of the object normalized to the wavelength inside the object, i.e. $L_{\max}/\lambda_{\mathrm{mat}}$. Since we have chosen a fixed dimension of the object, this normalized dimension $L_{\max}/\lambda_{\mathrm{mat}}$ only depends on the variation in the wavelength inside the object. As shown in Fig. 5.2(a) and 5.2(b), the evolutions of the relative error with respect to increased $L_{\max}/\lambda_{\mathrm{mat}}$ for both sets of collocation points are approximately similar. It is shown that for larger wavelengths, thus smaller $L_{\max}/\lambda_{\mathrm{mat}}$, the relative error reduces since the electric field inside the object is better approximated with linear functions.

Since we have used the point matching method to solve the integral equation, the electric field at the collocation points is approximated the best. Therefore, we consider the error distribution inside the object for the two sets of collocation points. The error distribution for the collocation points chosen at the vertices and at the center are shown in Fig. 5.3(a) and 5.3(b), respectively. These distributions are calculated for $L_{\max}/\lambda_{\mathrm{mat}}$=0.151 which corresponds to a wavelength of the electric field inside the object of $\lambda_{\mathrm{mat}} = L_{\max}/0.151 = 6.62$ m and a free-space wavelength of $\lambda_0 = L_{\max}/0.1 = 10$ m. In Fig. 5.3 is shown that the lowest errors are obtained at the observation positions which coincides with the different collocation points. This was expected since a property of the used solution method is that the field is approximated the best at a discrete set of points. Comparison of the two error distributions in Fig. 5.3 shows that the maximum error is approximately equal and that the largest errors are observed at positions with the largest distance from the collocation points. For these positions, the linear approximated electric field has the largest difference with the exact electric field as a consequence of the point matching method.

To get some measure for the error over the domain of the object, we introduce the mean

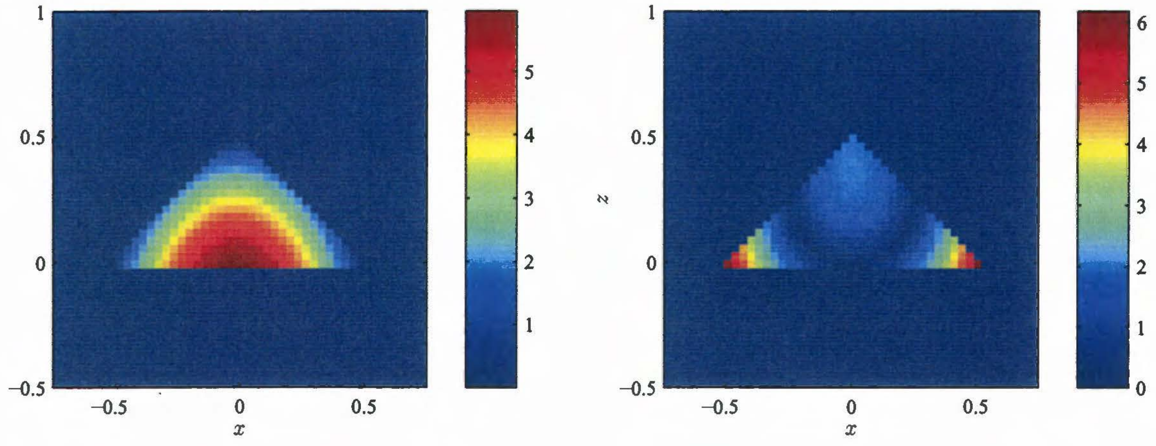

(a) (b)

Figure 5.3: Relative error [%] distribution for collocation points (a) at the vertices and collocation points (b) at the centers of the edges for dielectric object with $n_{\text{mat}} = 1.51$ and $\lambda_0 = 10$ m.

relative error which is defined as

$$\sigma_{\text{mean}} = \frac{1}{N_D} \sum_{\mathbf{r}_T \in D} \sigma(\mathbf{r}_T) \tag{5.2}$$

where $N_D = N_x \times N_z$ is the total number of observation positions inside domain D. For the two sets of collocation points, the mean relative error as function of the normalized maximum dimension $L_{\text{max}}/\lambda_{\text{mat}}$ is shown in Fig. 5.4. As shown in Fig. 5.4(b) the mean relative error for collocation points chosen at the centers of the edges is significantly lower than the mean relative error for collocation points chosen at the vertices, as in Fig. 5.4(a). The reason for this is that the approximation of the electric field solved for collocation points at the vertices over a larger area of the object differs from the reference field.

As a consequence of all the considerations above, in the next configurations we will use collocation points at the centers of the edges since this gives the lowest errors. In the discussed experiments we have varied only the wavelength of the electric field inside the object, but for a fixed wavelength of the electric field in free space, the error increases for a larger magnitude of the refractive index. This can be explained by the fact that the wavelength of the field in matter is related to the material properties, i.e. $\lambda_0 = n_{\text{mat}}\lambda_{\text{mat}}$. If the wavelength of the electric field in free space is much larger than the maximum dimension of the object with relative low refractive index, the electric field inside the object can be quite well approximated with linear functions. Therefore, in the next sections we use the wavelength in free space λ_0 which is at least ten times the maximum dimension of the object ($\lambda_0 > 10L_{\text{max}}$) since we will use dielectric objects with relative low refractive index ($n_{\text{mat}} = 1.51$). This suffices the condition $\lambda_{\text{mat}} \gg L_{\text{max}}$.

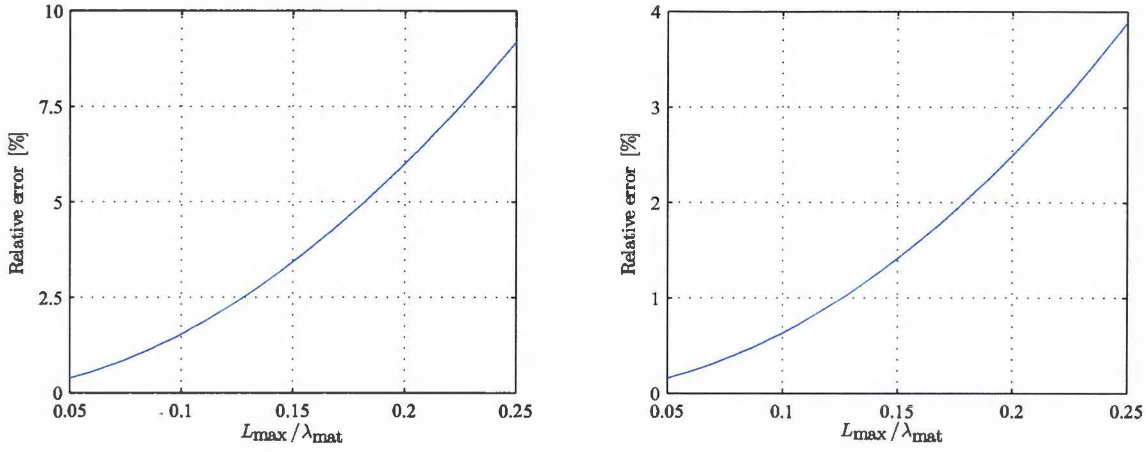

(a) (b)

Figure 5.4: Mean relative error [%] for collocation points (a) at the vertices and (b) at the centers of the edges for the dielectric object with $n_{\text{mat}} = 1.51$.

5.1.3 Electric far-field

Next, we consider the scattered electric field far away from the object. In the far-field region, the scattered electric field as derived in Section 3.2 is given by

$$\hat{E}_y^s(\mathbf{r}_T) = \Gamma_0(\mathbf{r}_T)\Psi(\theta) \tag{5.3}$$

where

$$\Psi(\theta,\psi) = \chi_e \iint_D \exp(-i\mathbf{k}_T \cdot \mathbf{r}_T')\hat{E}_y(\mathbf{r}_T'))dA' \tag{5.4}$$

is the radiation pattern and $\Gamma_0(\mathbf{r}_T)$ represents the equivalent line source. We recall that the normalized contrast function χ_e is defined as $\chi_e = n_{\text{mat}}^2 - 1$. To calculate the scattered field, we use the cylindrical object with triangular cross section (see Fig. 5.1) placed at the origin, see Fig. 5.5. In Fig. 5.5, the angle of incidence of the incident electric field is denoted by ψ and the angle of observation is denoted by θ. The distance between the object at the origin and the observation position, indicated by O, is fixed and large, i.e. $|\mathbf{r}_T| \gg 1$, such that the expression in Eq. (5.3) is valid. For this large distance, the value of the equivalent line source, contributing to the scattered electric field, is approximately constant. The variations in the scattered electric field are thus only due to the contributions of the radiation pattern. Therefore, in this chapter we compute only the radiation pattern since this quantity contains the most relevant information.

We define $\Psi^{\text{ref.}}$ and $\Psi^{\text{approx.}}$ as the reference radiation pattern and the approximated radiation pattern, respectively. To compare the radiation patterns, the following error measure is defined

$$\sigma_{\text{rad.}}(\theta,\psi) = \frac{\left|\Psi^{\text{ref.}}(\theta,\psi) - \Psi^{\text{approx.}}(\theta,\psi)\right|}{\left|\Psi^{\text{ref.}}(\theta,\psi)\right|} \times 100. \tag{5.5}$$

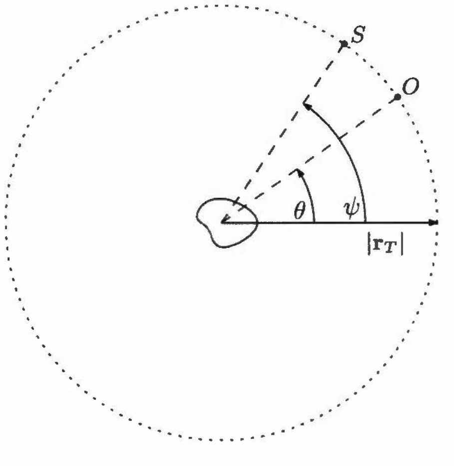

Figure 5.5: Far-field domain with angle of incidence Ψ and angle of observation θ.

The modulus and phase of the radiation pattern and the errors between the reference method and approximated method in Fig. 5.6 are shown for two wavelengths of the incident electric field. In Fig 5.6 (a,c,e) we have used a wavelength in free space of $\lambda_0 = 10$ m and in Fig. 5.6 (b,d,f) we have used a wavelength in free space of $\lambda_0 = 15$ m. The angle of observation is varied from 0° to 360° in 50 equal steps. In this case we use a fixed angle of incidence, namely $\theta = 0°$.

In Fig. 5.6 (a-b), the modulus of the reference radiation pattern and the approximated radiation pattern are approximately equal. For large wavelengths, the modulus of the radiation pattern is approximately equal to the area of the object (Area(D)) multiplied by the contrast function (χ_e), i.e. $|\Psi| \approx \chi_e \times \text{Area}(D)$. This can be deduced from Eq. (5.4) for large wavelengths. For the given object, the modulus of the radiation pattern is then equal to $|\Psi| = 1.2801 * 0.25 = 0.32$. This is in good agreement with the computed data as shown in Fig. 5.6 (a-b). As shown, the modulus of the radiation pattern corresponding to the largest wavelength $\lambda_0 = 15$ m in free space is approximated the best.

For the phase of the radiation patterns in Fig. 5.6 (c-d) are no significant difference observed. The relative error for the two wavelengths are shown in Fig. 5.6 (e-f). Comparing these two cases, shows that the relative error is larger for smaller wavelengths of the electric field. This is (again) attributed to the approximation of the electric field inside the object by linear functions. The differences in the relative error with respect to the variation in the wavelengths λ_0, found in Fig. 5.6, are in accordance with the results as obtained in Section 5.1.2. As shown in Fig. 5.6, for the two different wavelengths the relative errors are in the range of 0.004-0.16 %. Compared to the error in the electric field inside the object, the error in the radiation pattern is reduced.

Next, for the given object, we vary the angle of incidence Ψ and the angle of observation θ between 0° and 360° in 50 equal steps. The modulus and the phase for the approximated radiation pattern are shown in Fig. 5.7 (a) and (b), respectively. We used the wavelength in free space of $\lambda_0 = 10$ m and the object is made of a dielectric with refractive index $n_{\text{mat}} = 1.51$. In Fig. 5.7(c), the relative error between the reference and approximated radiation pattern is shown. The relative error is found in the range of 0.08-0.18% which is really small such that the

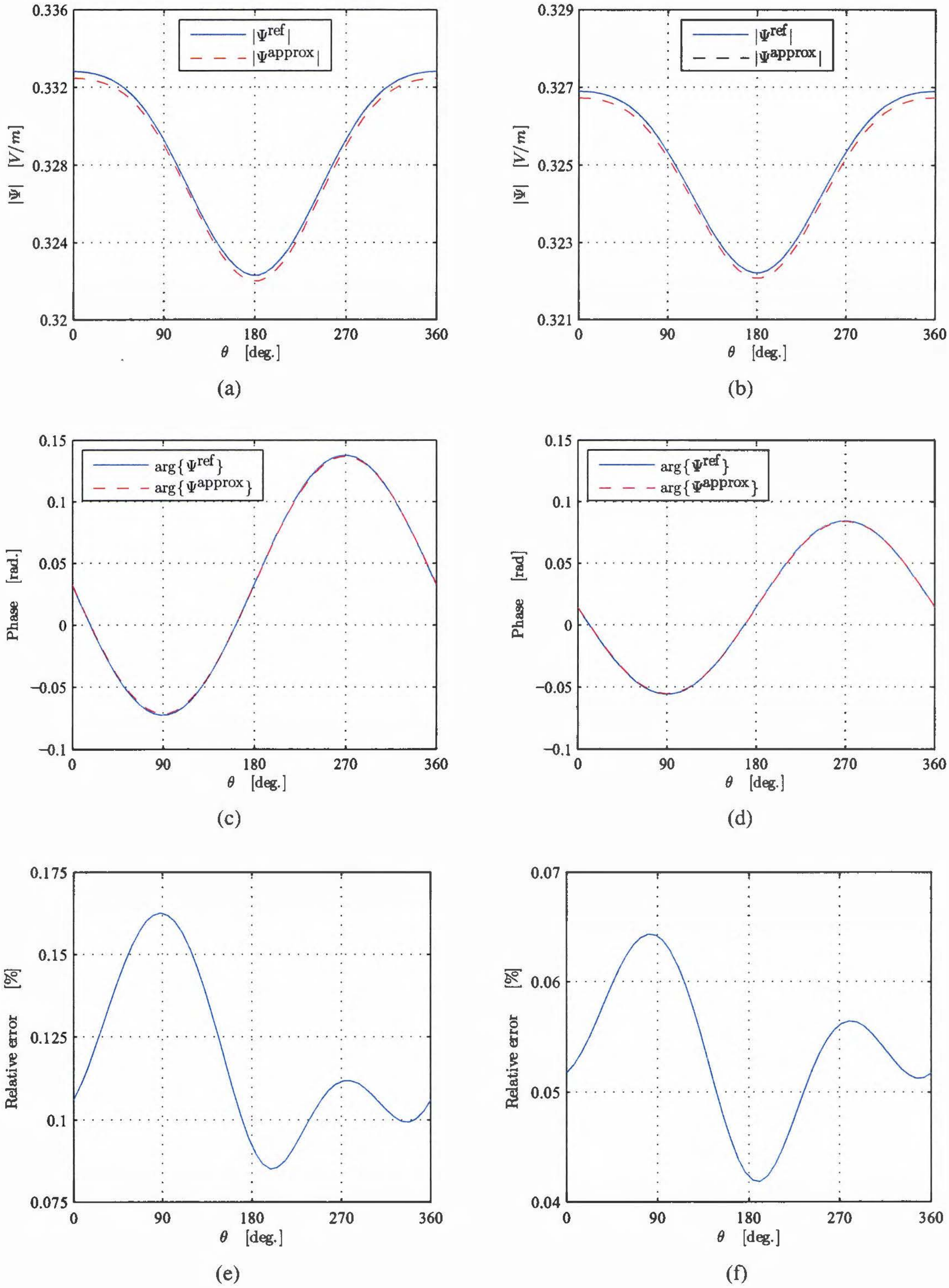

(a) (b)

(c) (d)

(e) (f)

Figure 5.6: Modulus, phase and relative error [%] of the reference and approximated radiation pattern for a dielectric object with triangular cross section with $n_{\text{mat}} = 1.51$ and angle of the incident electric field $\Psi = 0$ and wavelength in free space in (a,c,e) $\lambda_0 = 10$ m and in (b,d,f) $\lambda_0 = 15$ m.

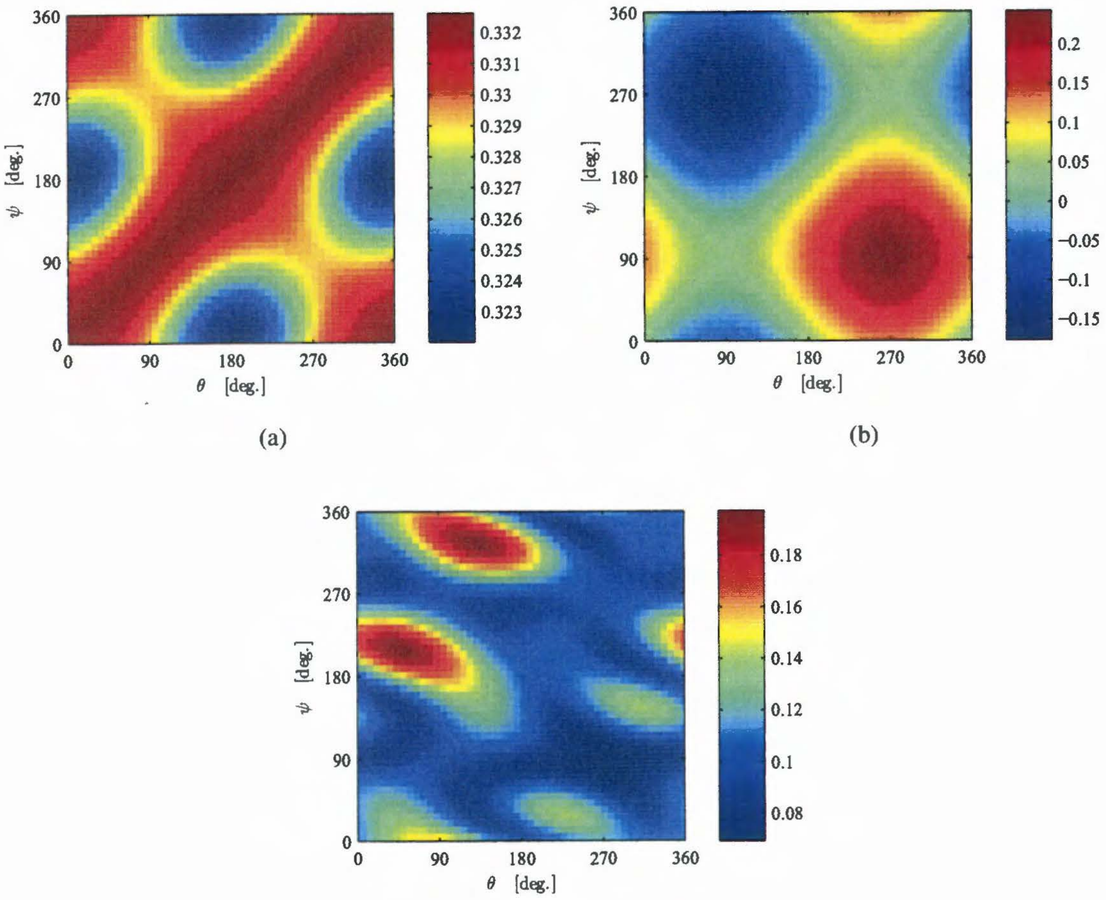

(a)

(b)

(c)

Figure 5.7: Approximated radiation pattern Ψ^{approx} as function of the angle of the incident electric field ψ and angle of observation θ for the dielectric object with triangular cross section and wavelength of free space $\lambda_0 = 10$ m. (a) Modulus radiation pattern, (b) phase radiation pattern and (c) relative error [%] between reference and approximated radiation pattern.

approximated electric far field resembles the exact electric field very closely.

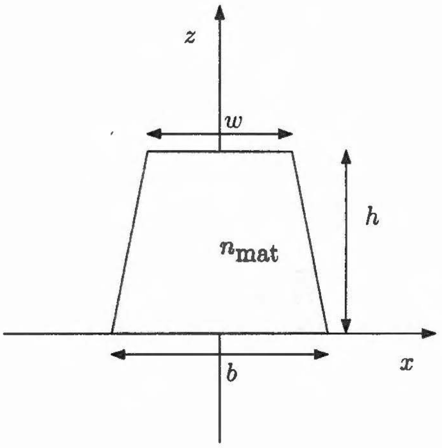

Figure 5.8: Dimensions of trapezoidal shaped cross section of the infinitely long cylindrical dielectric object.

Trapezium

So far, we have only considered an infinitely long cylindrical object with a triangular cross section. To demonstrate that also other geometries are suitable for the developed method we consider now an object with a trapezoidal cross section. The trapezoidal domain may therefore be decomposed into two triangular domains since the electric field inside the object is constructed with expansion functions which have a support only over a triangular domain. This means that the electric field is now expanded in 6 linear functions, i.e. 3 for each triangular subdomain. We start with an object with the cross section dimensions as shown in Fig. 5.8 having height $h = 1$ m, width $w = 1$ m and bottom width $b = 1$ m. The modulus, phase and the relative error for the approximated radiation pattern are shown in Fig. 5.9. The results are computed with the wavelength in free space of $\lambda_0 = 15$ m and the refractive index of the dielectric object is $n_{\text{mat}} = 1.51$. We observe that the mean value of the modulus of the radiation pattern is approximately equal to the contrast function multiplied by the area of the cross section of the object. The relative error between the reference radiation pattern and the approximated radiation pattern is in the order of 0.1 %. These errors are small and comparable with the errors found in the radiation pattern for an infinitely long object with triangular cross section.

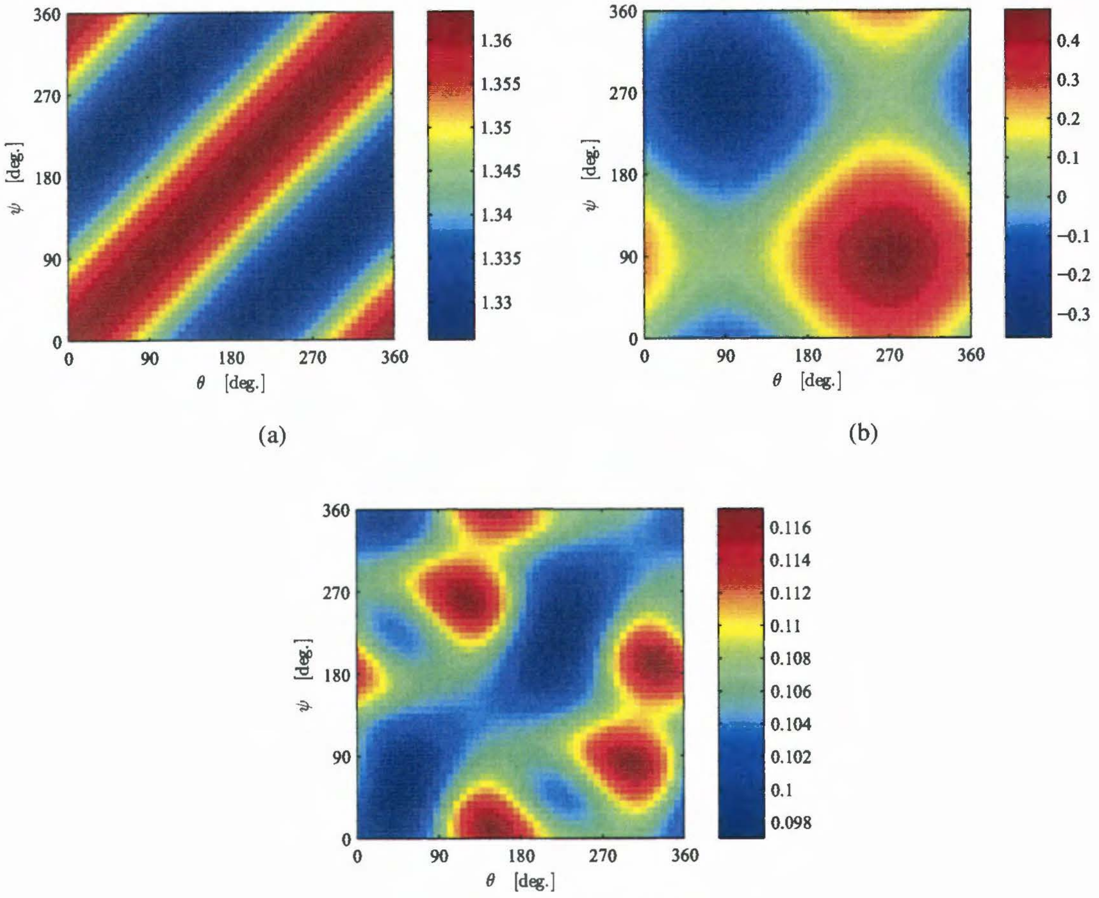

(a)

(b)

(c)

Figure 5.9: Approximated radiation pattern Ψ^{approx} as function of the angle of the source ψ and angle of the observation θ for object with rectangular cross section ($w = h = b = 1$ m.) with an incident electric field with wavelength $\lambda_0 = 10$ m. (a) Modulus radiation pattern, (b) phase radiation pattern and (c) relative error [%] between reference and approximated radiation pattern.

5.1.4 Reconstruction

In the last sections, we have shown that the relative error between the approximated radiation pattern and the reference radiation pattern is very low. These low errors suggest that from the radiation pattern it may be possible to retrieve information with respect to the structure geometry. For large wavelengths of the electric field inside the object, we have concluded that the modulus of the radiation pattern is approximately equal to the product of the contrast function and the area of the cross section of the object. In this thesis, the material properties of the object are known and thus the contrast function is known. It means that given the contrast function, the area of the cross section of the object can be retrieved from the modulus of the radiation pattern. The computed modulus gives a rough estimate of the area of the object. This information can be used as a start guess in inversion methods for exact retrieval of the geometrical parameters of the object. To retrieve the different geometrical parameters accurately, the variations in the radiation pattern contain the most valuable information. To illustrate this, we consider the following example.

In Fig. 5.10, two radiation patterns corresponding to two different objects with a trapezoidal cross section with equal area, i.e. Area $= 0.855$ m^2, are shown. The geometrical parameters of the two objects can be found in Table 5.1. The radiation patterns are computed with the approximated method and we have used a free-space wavelength $\lambda_0 = 15$ m and the object consist of a material with refractive index $n_{\text{mat}} = 1.51$.

	h [m]	w [m]
case A	0.9	0.9
case B	0.855	1.0

Table 5.1: Dimensions of two objects with equal areas (Area = 0.855 m^2) of the cross section of object and fixed bottom width $b = 1$ m.

As shown in Fig. 5.10, the modulus of the two radiation patterns differs only very little. The areas of the cross section of the object reconstructed from these radiation patterns are approximately equal. This means that although the two objects seems equal on basis of the value of the area, they differ in shape. Other techniques are then necessary to retrieve the geometrical parameters of the object.

Therefore, we formulate the problem as an inverse-scattering problem where we have to solve the following minimization problem

$$\min_{\mathbf{p}\in\{\mathrm{w,h}\}} F(\mathbf{p}) \tag{5.6}$$

where $F(\mathbf{p})$ is the objective function defined as

$$F(\mathbf{p}) = \sum_{\theta_n,\Psi_n\in\{0,360^\circ\}} \frac{1}{2}||\Phi^{\text{ref.}}(\mathbf{p},\theta_n,\Psi_n) - \Phi^{\text{approx.}}(\mathbf{p},\theta_n,\Psi_n)||^2 \tag{5.7}$$

where we vary the angle of incidence Ψ and observation θ between 0°-360° in 50 equal steps. Next, the aim is to retrieve the two geometrical parameters (w and h) of the in table 5.1 defined

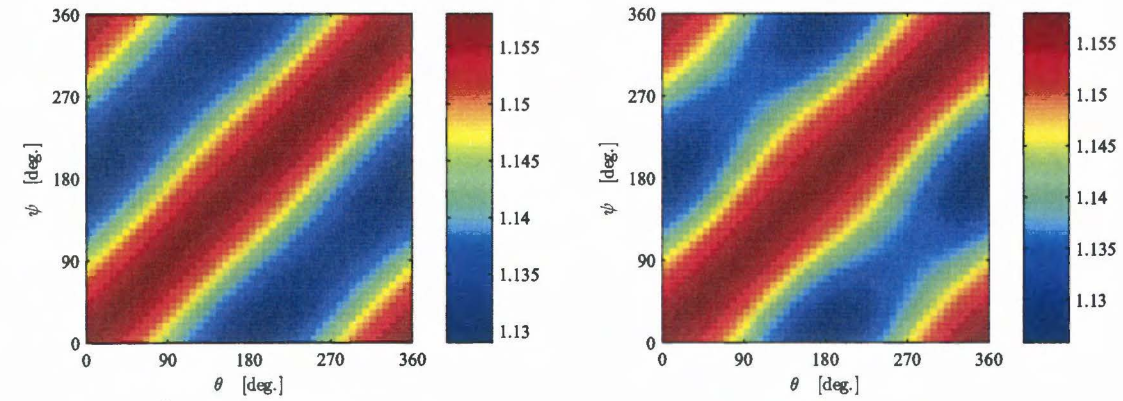

(a) (b)

Figure 5.10: Radiation pattern for two objects with equal area Area=0.855m^2. (a) Case A: $h = 0.9$ m, $w = 0.9$ m. (b) Case B: $h = 0.855$ m, $w = 1$ m and fixed bottom width $b = 1$ m for both cases.

objects from the reference measured data. To avoid 'inverse crime', we treat the data from the reference method as the reference measured data and our data as the approximated computed data.

First we consider case A with height $h = 0.9$ m, width $w = 0.9$ m and bottom width $b = 1$ m. We start with computing the objective function by varying the width w and keeping the height h fixed. The objective function is shown in Fig. 5.11(a). In a similar manner the width is fixed and the height is varied and the results is shown in Fig. 5.11(b). For the two individual parameters (w, h) a minimum for the objective function is found. As shown, when one geometrical parameter is fixed, the other parameter can be accurately retrieved. Both parameters are reconstructed with a relative error of 0.4-0.9%.

Next, we vary the width w and the height h at the same time to simultaneously retrieve information about the two parameters (w, h) of the object. The objective function with respect to the width w and the height h is shown in Fig. 5.12. As shown, multiple local minima are found and the global minimum corresponds to a width $w = 0.908$ m and a height $h = 0.9$ m. Compared to the reference object, the height h is exactly retrieved and the error in the width w is $\approx$0.9%. When considering the local minima it is found that they are aligned on a line for which the total area of the cross section of the object is approximately constant (see Fig. 5.12(b)).

In a similar manner, we have reconstructed the geometrical parameters for the second object, i.e. case B where the height $h = 0.855$ m, the width $w = 1$ m and the bottom width $b = 1$ m. The reconstructed parameter values for case A and case B are tabulated in Table 5.2. The width and height parameters corresponding to the minimum of the objective function are indicated by the subscript $_{\text{opt}}$. Experiments have shown that the behavior of the objective function for case B is comparable with case A, thus the local minima in the objective function are (again) found along a line corresponding to a constant area. As shown in Table 5.2, for the two cases the differences

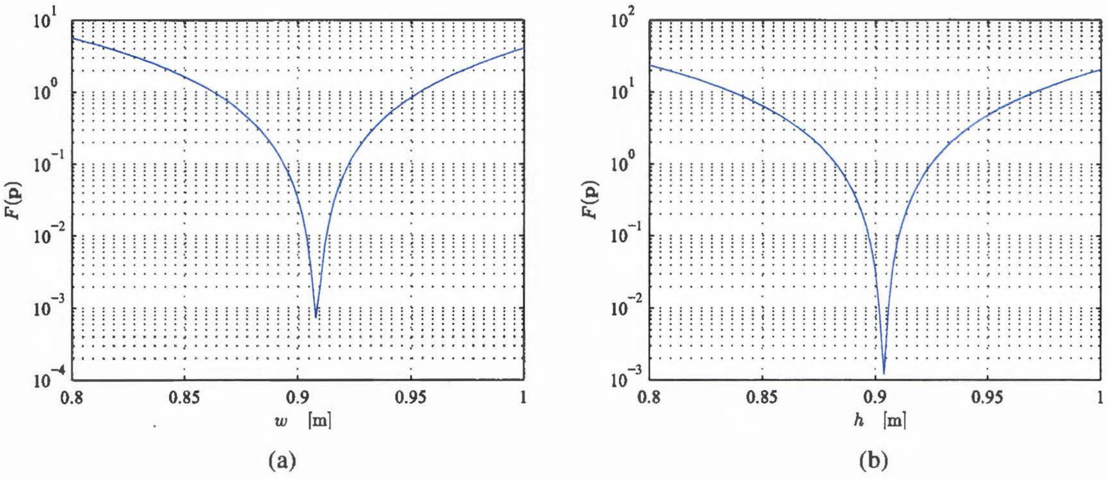

Figure 5.11: Objective function $F(\mathbf{p})$ as function of (a) the width w for fixed height h, (b) and as function of the height h with fixed width w.

in the parameters are approximately equal.

	h_{opt} [m]	w_{opt} [m]	max relative error [%]
case A	0.908	0.900	0.93%
case B	0.854	1.000	0.04%

Table 5.2: Reconstructed parameters for two objects, case A and case B and maximum relative error [%].

In summary, we can conclude that we can reconstruct the shape of the object, accurately if the material properties of the object are given. This is only the case when the wavelength of the electric field inside the object is large compared to the maximum dimension of the cross section of the object. We have observed that the local minima in the objective function are found along a line for which the area is constant. This information can be used to increase the speed of the reconstruction process. Therefore, we propose the following reconstruction strategy: in the first step we consider a rectangular cross section $w = h = b$ and vary the dimension of the rectangle until a global minimum is found. Therefore, only one parameters should be optimized. Within a small number of minimization steps the area of the rectangular can be retrieved. Next, the individual width and height can be found in more steps precisely using the value of dimensions (w, h, b) of the rectangular object as starting point. Therefore more advanced optimization techniques are necessary to increase the speed of the reconstruction process.

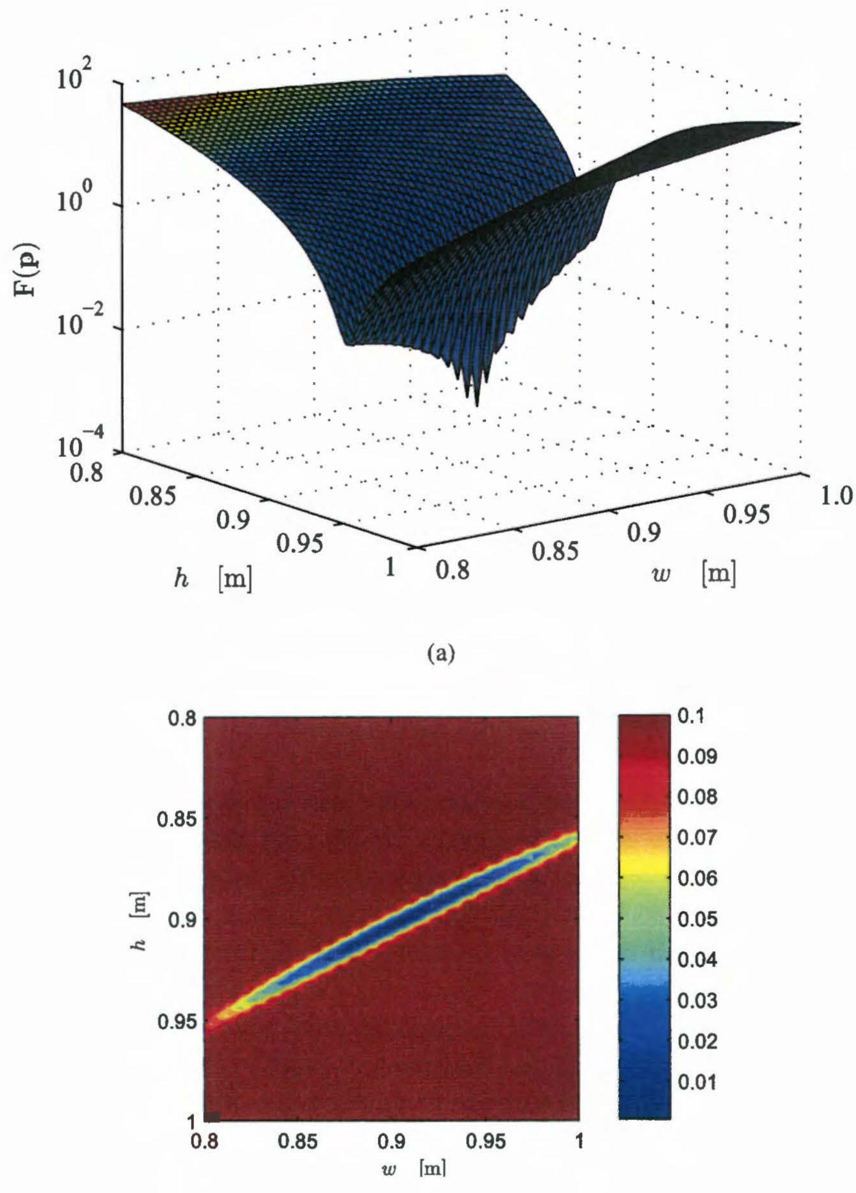

(a)

(b)

Figure 5.12: Objective function $F(\mathbf{p})$ as function of the width w and the height h.

5.2 Diffraction Gratings

In this section, we consider the diffraction of electromagnetic plane waves by a diffraction grating which is periodic in one direction.

The diffraction grating under consideration is invariant along the y-direction and is composed of a lower half space ($z < 0$) consisting of a homogeneous medium with complex refractive index. The upper half space ($z \geq 0$) consist of free space. Additionally, a structure periodic along the x-direction is included in the upper half space. This structure is made of medium with a complex refractive index. One period of the cross section of the grating with an object in the upper half space with a trapezoidal shape is shown in Fig. 5.12. The grating is illuminated by an electrically polarized plane wave $E_y^p \mathbf{u}_y$ with an angle of incidence lying in the transverse plane. This means that we consider only the planar diffraction. The region of interest lies in the upper half space since this is the region where the electromagnetic field or related quantities can be detected and measured.

5.2.1 Reference program: RCWA

To validate the electric field formulation for the diffraction grating with the method derived in Chapter 4, we use the rigorous coupled-wave analysis (RCWA) method [2]. In the RCWA method the electromagnetic field is found from rigorously solving Maxwell equations. The core of this method is the assumption that the field above and below the periodic structure can be described by a Rayleigh expansion. The amplitudes corresponding to the reflected and transmitted fields can be found by applying the boundary conditions to the expression of the field inside the periodic structure. For structures periodic in one direction and with arbitrary shape, the refractive index of the material depends on two spatial coordinates. Therefore, the periodic structure is modeled as a stack of lamellar gratings, thus divided in M layers in the direction perpendicular to the periodicity of the grating. The field inside each layer is expanded in a Fourier series where the series is truncated by a finite number of terms or harmonics. For each layer, an algebraic eigenvalue system is found. The coupling between the different layers is accomplished by ensuring that the continuity of the tangential components of the electromagnetic field at the interface between successive layers is satisfied. This results in a large system of linear equations that can be solved by matrix inversion. We consider further the results obtained with the RCWA method as the reference solution.

5.2.2 Diffraction efficiency

To compare the results obtained with the reference method and with the approximated method discussed in Chapter 4 we will introduce a measure known as the diffraction efficiency. The diffraction efficiency for a given spectral order is defined as the ratio of the reflected power and of the incident power through the surface parallel to the mean plane of the grating [16]. The spectral orders are an effect of the with an electromagnetic field illuminated diffraction grating since this leads to a discrete number of reflected waves. This was shown in Chapter 4, where for the electric field a Floquet modal expansion was used and the modal coefficients or

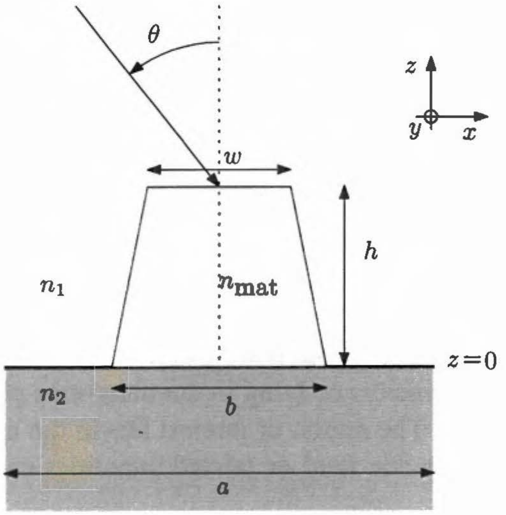

Figure 5.12: Cross section of one period of the diffraction grating.

case	n_{mat}	n_2
1	1.51+0.00i	1.51+0.00i (resist)
2	1.51+0.00i	3.77+0.01i (silicon)
3	1.51+0.00i	0.22+6.71i (metal)
4	3.77+0.01i	3.77+0.01i
5	0.22+6.71i	0.22+6.71i

Table 5.3: Material compositions of the diffraction grating.

reflection coefficients were derived. We define the diffraction efficiencies related to the reflection coefficients as follows

$$\mathrm{DE}_n = R_n R_n^* \mathrm{Im}\left(\frac{\gamma_{1n}}{k_0 n_1 \cos(\theta_i)}\right) \tag{5.8}$$

where n is the order of the diffraction efficiency and R_n^* is the complex conjugated of R_n.

Next, we compute the diffraction efficiencies for five different material compositions of the diffraction grating. The numerical values of the refractive index of the periodic object and the lower half space are shown in Table 5.3. As shown, the grating is composed of a combination of resist, silicon and metal as indicated between the brackets in Table 5.3. The geometrical parameters are defined by the width w, height h, bottom width b and the periodicity length a. We use for the grating configuration the following parameters $w = h = b = 1$ m and $a = 2$ m. The diffraction efficiencies computed with the reference method and with the approximated method are now compared. We define the maximum relative error in the diffraction efficiency as

$$\sigma_{\mathrm{DE}}^{\max} = \max_{\theta_i \in (0,45)} \frac{|\mathrm{DE}_0^{\mathrm{ref}}(\theta_i) - \mathrm{DE}_0^{\mathrm{approx}}(\theta_i)|}{\mathrm{DE}_0^{\mathrm{ref}}(\theta_i)} \times 100\% \tag{5.9}$$

where the angle of the incident field θ_i is varied between 0° and 45° since at these angles the diffraction efficiencies can be measured by a detector. In Eq. (5.9), the reference diffraction efficiency is indicated by $^{\mathrm{ref}}$ and the approximated diffraction efficiency by $^{\mathrm{approx}}$. For the given geometrical parameters, only zero-order diffraction orders are present for $\theta_i \in (0, 45)$. This can be understood from the definition of γ_{1i} which is only imaginary when $n = 0$. Hence, the maximum relative error for the zero-order diffraction efficiencies as function of the free-space wavelength are shown in Fig. 5.14 for the five different material compositions of the grating. The scattered electric field is found from solving the integral equation with a truncated series with $n \in$

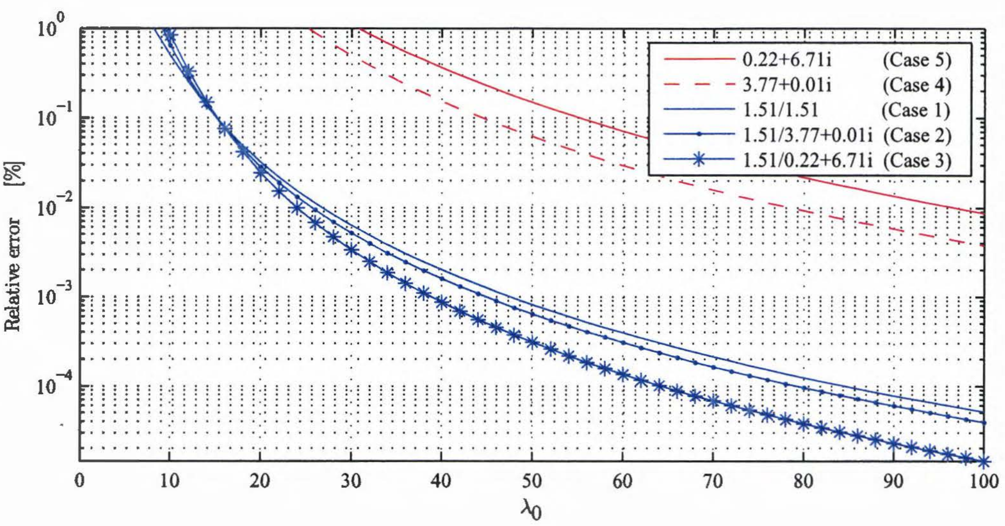

Figure 5.14: Maximum relative error [%] in zero-order diffraction efficiencies DE_0 as function of the wavelength in free space for five different compositions of the material of the diffraction grating. The used geometrical parameters of the grating are $h = w = b = 1$ m and $a = 2$ m. The approximated diffraction efficiencies are computed with $T = 5$ terms in the series evaluation of the scattered electric field. For the RCWA results $M = 10$ layers and $(2N + 1) = 21$ harmonics are used.

$(-N, N)$ in the secondary electric field in Eq. (4.35). The approximated diffraction efficiencies are computed with $T = 5$ terms ($T = 2N + 1$) in the series. The RCWA diffraction efficiencies are computed with $M = 10$ layers and $(2N + 1) = 21$ harmonics. As shown in Fig. 5.14 for a given relative error, the free-space wavelength differs for the five considered cases. This is a direct consequence of the used material properties. As mentioned in the previous section, the wavelength of the electric field inside the object depends on the refractive index. It means that the wavelength of the electric field inside the object should be at least 4 times the maximum length of the object if the electric field has to be approximated by linear functions. For the given diffraction grating, the electric field is approximated with linear function only in the periodic structure in the upper half space. We know that the relation between the free-space wavelength λ_0 of the incident field and the wavelength inside the object is found by $\lambda_{\text{mat}} = \lambda_0/\text{Re}\{n_{\text{mat}}\}$. For the refractive index only the real part depends on the wavelength inside the object since this part corresponds to propagating waves. When we compute the corresponding wavelengths inside the object for case 1, case 2 and case 3 for a fixed relative error, it is observed that wavelength inside the object is approximately equal. This is in accordance with the expectations. The difference in the diffraction efficiencies between case 1, case 2 and case 3 are due to the material properties of the lower half space. The effects of the lower half space are evaluated analytically as shown in Eq. (4.35). As shown in Fig. 5.14 the lower half space has a small influence on the error in the diffraction efficiencies. It is obvious that the error in the diffraction efficiencies can be reduced by increasing the wavelength of the incident electric field in free space. Therefore, the wavelength of the electric field inside the object is larger so that the electric field is better approximated with linear functions.

When the diffraction grating is made of metal, i.e. case 5, the imaginary part of the refractive index is much larger than the real part of the refractive index. The physical interpretation of an imaginary refractive index is that the field decreases exponentially according to $\exp(-k_0\mathrm{Im}\{n_{\mathrm{mat}}\}|z|)$. It means that the exponentially decreasing behavior of the electric field may be approximated with linear functions only when the argument of the exponential function is small. Since the imaginary part of the refractive index is large, the wavelength of the incident electric field should be large to get a small free-space wavenumber k_0. This is shown in Fig. 5.14, where for the case of a metal grating similar relative errors are observed for much larger wavelengths λ_0 compared to the other material compositions of the grating.

Next, we consider the effects of variations in the width w and height h for the diffraction grating as defined in case 1 on the diffraction efficiencies. For this we use a fixed wavelength in free space $\lambda_0 = 15$ m, a fixed bottom width $b = 1$ m and a fixed length of one period of the grating $a = 2$ m. The numerical results for the zero-order diffraction efficiencies computed with the RCWA method and the approximated method for three different angles of the incident electric field can be found in Table 5.4. In the approximated method, the electric field is solved with the evaluation of only one term ($T = 1$) in the expression for the scattered electric field in Eq. (4.35). Higher-order terms in the scattered electric field decrease exponentially for the given geometrical parameters of the diffraction grating and may therefore be neglected. In the evaluation of the diffraction efficiencies using the RCWA method, the periodic structure in the diffraction grating is divided in a stack of lamellar gratings. This means that the number of layers, which are used to approximate the grating, depends on the shape of the object in the upper half space. When there is a large difference between the top width and the bottom width of the trapezoidal object a larger number of layers are necessary. In the next results, we use $M = 10$ layers and $(2N + 1) = 21$ harmonics in the RCWA method since this results in low errors in the diffraction efficiencies.

		RCWA	Results		Our	Results	
h [m]	w [m]	$\theta = 0°$	θ=22.5°	θ=45°	$\theta = 0$	θ=22.5°	θ=45°
1.0	1.0	0.03126	0.04748	0.07953	0.03129	0.04753	0.07960
0.8	1.0	0.03466	0.05161	0.08469	0.03469	0.05165	0.08475
1.0	0.8	0.03194	0.04831	0.08057	0.03184	0.04817	0.08034
0.8	0.8	0.03513	0.05217	0.08539	0.03507	0.05209	0.08525

Table 5.4: Diffraction efficiency DE_0 for case 1 ($n_2 = n_{\mathrm{mat}}$=1.51) with $\lambda_0 = 15$ m, $T = 1$ and $M = 10$ layers and $(2N + 1) = 21$ harmonics (RCWA).

In the first row of Table 5.4, the height h and the width w are both equal, i.e. $h = w = 1$ m. As shown, the differences in the zero-order diffraction efficiencies between the RCWA results and the approximated results are observed in the third digit corresponding to a relative error in the order of 0.1%. For the given wavelength of the electric field in free space, this relative error is in accordance with the results in Fig. 5.14. When the height h and the width w are varied, in rows

2-4 in Table 5.4, the relative error in the diffraction efficiencies increases. The relative errors are then found in the range of 0.1-0.2%. The differences in the diffraction efficiencies in Table 5.4 are all caused by the assumption that the electric field inside the object can be approximated by linear functions. The differences between the actual electric field inside the object and the approximated electric field lead to an error in the diffracted field and finally in the diffraction efficiencies. Hence the error is related to the maximum dimension of the trapezoid, the material properties and the wavelength in free space.

As already mentioned, the truncation of the series for the evaluation of the integral equation has little influence on the scattered electric field for the above discussed configuration. To distinguish between the errors due to the influence of the linear approximation of the electric field and errors due to the truncation of the series, we consider the case where the period is chosen much larger than the maximum dimension of the object $a \gg L_{\text{max}}$. For the evaluation of the scattered electric field, a sum of closed-form two-dimensional Fourier integrals is used, see Eq. (4.35). These separate spatial Fourier transforms depends on $\gamma_{1n} = \sqrt{k_{xn}^2 - k_0^2 n_1}$ which has a contribution to the scattered electric field when the value of γ_{1n} is real and small or imaginary. Since γ_{1n} depends on $k_{xn} = k_{0x}^i + n\frac{2\pi}{a}$ which is small when $a \gg n$, the value of γ_{1n} is also small.

Therefore we consider a diffraction grating with dimensions $a = 10$ m, $h = w = b = 1$ m and the material properties as defined in case 1 ($n_{\text{mat}} = n_2 = 1.51$). The relative error in the diffraction efficiencies DE_0 and DE_1 as function of the number of terms in the evaluation of the scattered electric field are shown in Fig. 5.15. As shown, for this case more terms are needed to accurately solve the electric field and to obtain the corresponding diffraction efficiencies. The relative error is in the range of 0.1-7% for the first 15 terms, after which the relative error oscillates and finally reaches a stable point. This final relative error is fully caused by the difference in the linearly approximated electric field and the exact electric field.

5.2.3 Reconstruction

Finally, the aim of evaluating the diffraction efficiencies is to retrieve information about the structure from the measured data and thereby to reconstruct the shape of the trapezoidal cross section of the object. To facilitate this, we use a similar reconstruction strategy as we did for the non-periodic case. We define the objective function as

$$G(\mathbf{p}) = \sum_{\theta_n \in \{0,45^\circ\}} \frac{1}{2} || \text{DE}_0^{\text{ref.}}(\mathbf{p}, \theta_n) - \text{DE}_0^{\text{approx.}}(\mathbf{p}, \theta_n) ||^2. \tag{5.10}$$

Since we are restricted to observation positions in the upper half space, in Eq. (5.10) we vary the angle of incidence θ between 0° and 45° in 50 equal steps. We treat the RCWA data as the reference measured data, indicated by $^{\text{ref.}}$, and our data as the approximated computed data indicated by $^{\text{approx.}}$.

As an illustrative example, we consider the diffraction grating with width $w = 0.9$ m, height $h = 0.9$ m, bottom width $b = 1$ m, period $a = 2$ m and refractive index $n_{\text{mat}} = n_2 = 1.51$. We compute the objective function by varying the width w and keeping the height h fixed and vice versa. The results can be found in Fig. 5.16(a) and Fig. 5.16(b), respectively.

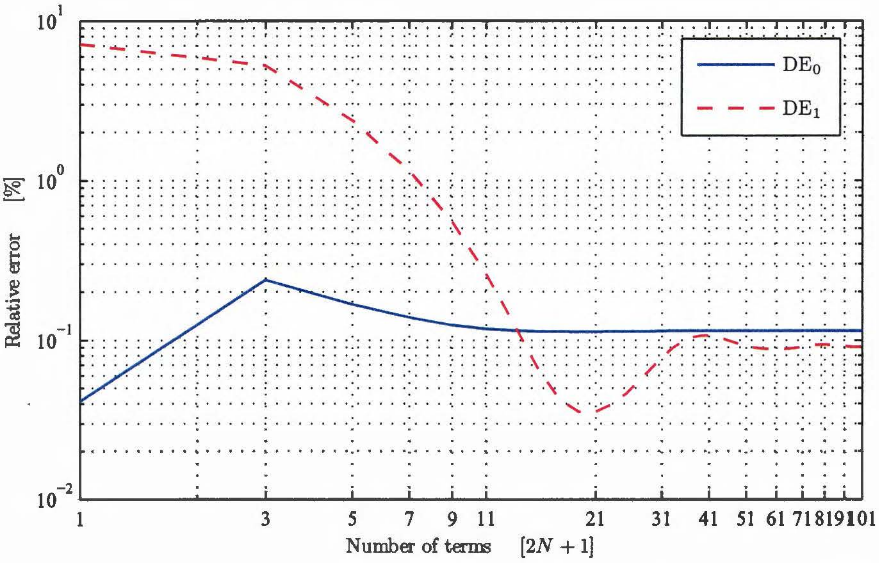

Figure 5.15: Relative error [%] as function of the number of terms for the diffraction efficiencies DE_0 and DE_1 for $\lambda_0 = 15$ m, $w = h = b = 1$m and $n_2 = n_{\text{mat}} = 1.51$.

For the two individual parameters (w, h) a (global) minimum for the objective function is found. This gives the optimal values for both the width and the height as presented in Table 5.5. Both parameters are reconstructed with a relative error of 0.2-3.8%. In Fig. 5.16 is shown that the maximum value of the objective function to variations in the height h is two orders $O(10^2)$ larger compared to the value of the objective function to variations in the width w. The minimum of both objective function are approximately equal. This means that a variation in the height has the largest effects on the objective function. Hence, the objective function is more sensitive to variations in the height h than to variations in the width w.

	value	G(**p**)	Relative error [%]
w_{opt}	0.866	1.7E-09	3.8%
h_{opt}	0.898	1.4E-09	0.2%

Table 5.5: Reconstructed parameters $\mathbf{p} \in (w, h)$ of the geometry and relative error for a grating with dimensions: $w = h = 0.9$ m, $b = 1$ m, $a = 2$ m, $n_{\text{mat}} = n_2 = 1.51$ and $\lambda_0 = 15$ m.

Next, we vary the width w and the height h at the same time to simultaneously retrieve information about the two parameters of the object. We use the similar reference trapezoid, i.e. $h = w = 0.9$ m. The objective function with respect to the two geometrical parameters (w, h) is shown in Fig. 5.17, where multiple local minima of the objective function can be observed. The lowest value of the objective function is found for $w = 0.952$ m and $h = 0.892$ m. The maximum relative error for the width reconstruction is ≈5.8% and for the height ≈0.9%. These values are summarized in Table 5.6. In Fig. 5.17 we observe again that the objective function is more sensitive to variations in the height.

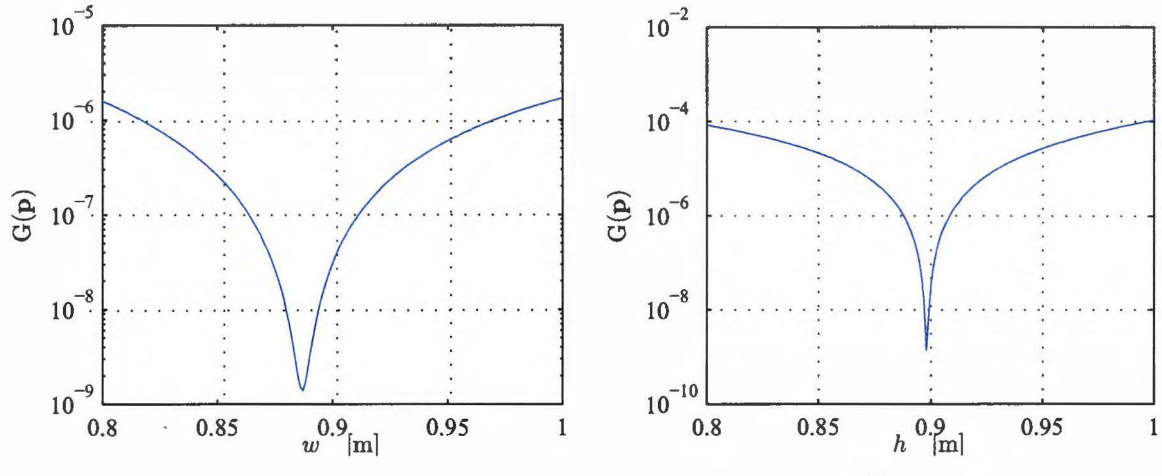

(a) (b)

Figure 5.16: Objective function $G(\mathbf{p})$ as function (a) of the width w when height h is fixed and (b) of the hight h when width w is fixed for reference trapezoid with $w = h = 0.9$ m, $b = 1$ m, $a = 2$ m, $n_{\text{mat}} = n_2 = 1.51$ and $\lambda_0 = 15$ m.

Therefore, the reconstruction strategy should be revised. Since the height is the parameter which has the largest effects on objective function, this is the parameter which should be reconstructed firstly. Once this parameter is found, the width can be subsequently found. As a final step, the two parameters can be varied at the same time to obtain a global minimum in the objective function, while it should be avoided that local minima are found. As shown in Fig. 5.18, the local minima are aligned on a straight line. Therefore, for a local minimum on this line the value of two neighboring local minima can be compared to asses that a global minimum is found.

w_{opt}	h_{opt}	G(p)	Relative error [%]
0.952	0.892	1.2E-11	0.9-5.8%

Table 5.6: Reconstructed values of the geometry for parameters $\mathbf{p} \in (w, h)$ of the grating and relative error for reference trapezoid with values $b = 1$ m, $w = h = 0.9$ m, $a = 2$ m, $n_{\text{mat}} = n_2 = 1.51$ and $\lambda_0 = 15$ m.

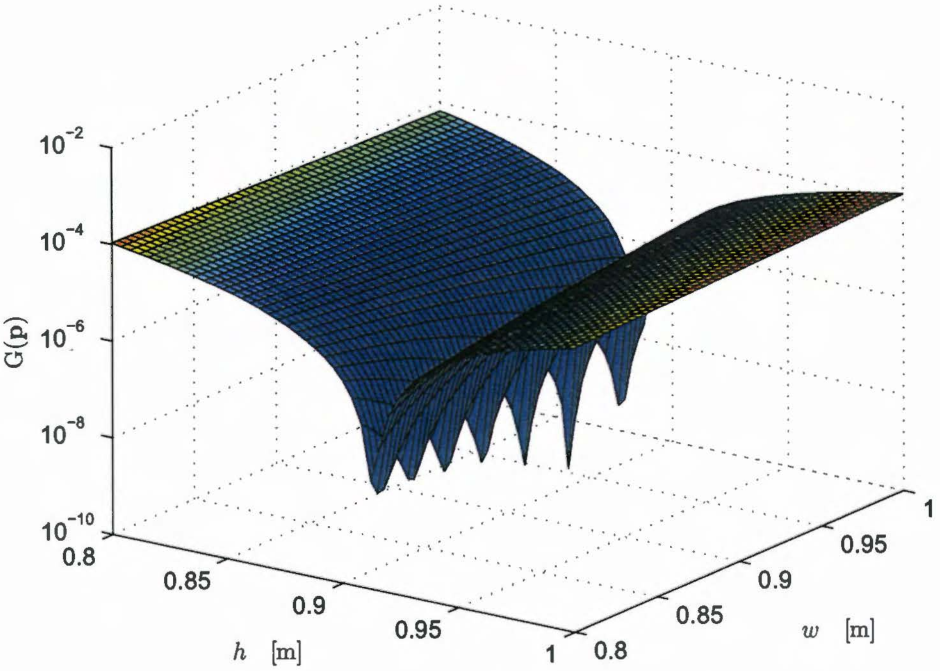

Figure 5.17: Objective function as function of the width and the height for reference object with geometry parameters $w = h = 0.9$ m, $b = 1$ m , $a = 2$ m for case 1 with $\lambda_0 = 15$ m.

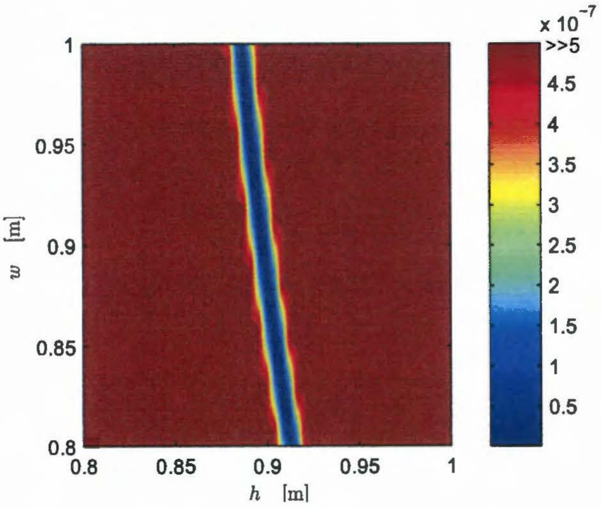

Figure 5.18: Contour graph for objective function Fig. 5.17.

Chapter 6

Conclusions and Recommendations

As formulated in the introduction, the objective of the thesis, was to find a fast and efficient solution method for the scattered electric field when a diffraction grating was illuminated by an electrically polarized plane wave. The diffraction gratings were made of a structure periodic in one direction and placed on the planar interface between two half spaces with different electromagnetic properties. The incident field was a plane wave electrically polarized along the invariant direction of the grating with an arbitrary angle incidence lying in the transverse plane.

Since a large part of the research was devoted to the formulation of the scattering problem we will discuss briefly the solution strategy. The scattering problem for the electric field was formulated in the form of a domain integral equation. In this formulation, the scattered electric field was expanded into an infinite series of Floquet modes. The corresponding Floquet modal coefficients were written in the form of a spatial Fourier transform where the domain of integration was restricted to one period of the diffraction grating. The electric field was found from solving the integral equation using the point matching method, a special case of the method moments where linear functions as basis functions and Dirac delta functions as test functions are used. On the assumption that the wavelength of the electric field inside the structure was large compared to the maximum dimension of one period of the periodic structure, the electric field inside the object can be approximated with linear basis functions. Via the point matching procedure, the integral equation reduces in a system of linear equations. In the evaluation of the system of equations, the occurring surface integral over the interior of the object are transformed in a sum of line integrals which encloses the boundary of the object.

In this thesis, we have first demonstrated the solution method for the case of an infinitely long dielectric cylinder with trapezoidal cross section embedded in free space. The object was illuminated by a plane wave electrically polarized in the invariant direction of the cylindrical object.

To find the best solution for the electric field inside the dielectric cylinder with triangular cross section, we have first investigated the influence on the choice of collocation points on the value of the electric field. Numerical computations have shown that the lowest relative errors in the electric field with respect to an alternative solution method are obtained for collocation points chosen at the center between two vertices for an object with triangular cross section. For a free-space wavelength λ_0 that is ten times the maximum dimension of the object ($\lambda_0 = 10L_{\text{max}}$) the mean relative errors, distributed over the domain of the object are below 2%. This is the case for objects with relative low electric contrast (in this example $n = 1.51$) since the wavelength in matter is related to material properties. For the electric far-field, even lower relative errors in the order of 0.5% are found for different observation and incidence angles.

From reference electric far-field data we have retrieved two geometrical parameters of the trapezoidal shaped object, i.e. the top width and the height, with the developed methods. The height was exactly found and the width was found with a relative error of 0.9%. The proposed reconstruction strategy was to retrieve the area of the cross section of the object within a small number of minimization steps after which the individual width and height can be found precisely with more iteration steps.

For diffraction gratings, we have considered periodic structures which are made of an array of infinitely long cylindrical objects placed at the interface between two half spaces. The cylindrical object had a trapezoidal cross section with a maximum width of 1 m, a maximum height of 1 m and the length of the one period was $a = 2$ m. We have investigated five different material compositions of the diffraction grating to compute the diffraction efficiencies. The used materials were resist ($n = 1.51$), silicon ($n = 3.77 + 0.01i$) and metal ($n = 0.22 + 6.71i$). We have shown that the electric field inside the grating depends on the electromagnetic properties of the structure. It means that the accuracy of the diffraction efficiencies depends on the wavelength of the incident electric field in free space and the material properties. This is in agreement with the expectations because we have assumed that the electric field inside the grating can be approximated with linear functions. From the numerical results found in Chapter 5 we may conclude that the diffraction efficiencies can be found with an accuracy of 99.9% when the wavelength of the electric field inside the periodic object is at least eight times the maximum dimension of the cross section of the object ($\lambda_{\text{mat}} > 8L_{\text{max}}$). Variations on the width and the height of the trapezoidal shape of the diffraction grating has a negligible effect on the error of the diffraction efficiencies. Under the condition that $\lambda_{\text{mat}} > 8L_{\text{max}}$, the electric field was solved with only one term in the integral equation because the truncation of the series for the evaluation of the scattered field has less influence on the error for gratings with periods smaller than the wavelengths as a consequence of the fast decaying exponentially kernel in the integral equation.

We have reconstructed two structure parameters, the top width and the height, with a relative error of 5.8% and we have shown that the objective function is two orders ($O(10^2)$) more sensitive for variations in the height than in the width. Therefore we argued that the reconstruction strategy should be revised. Firstly, the height should be retrieved since this has the largest effects on the objective function while at the second step the width should be retrieved.

The main advantage of the discussed approximated solution method is that the electric field is derived in a closed form which can be computed very fast. The corresponding geometrical parameters are found with limited accuracy. These parameters can be used as an initial estimate in more advanced but relative slower solution methods to find the exact parameters.

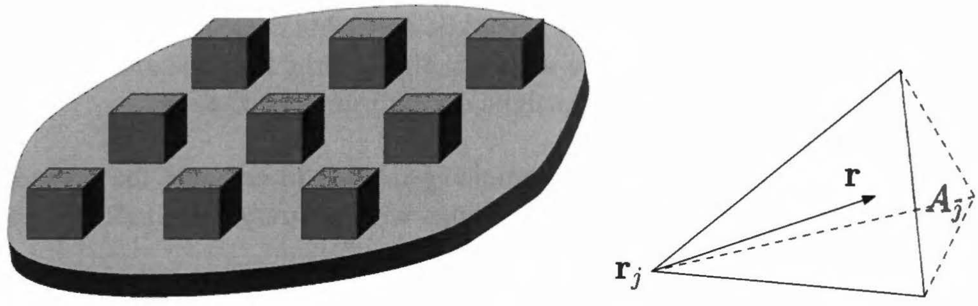

(a) (b)

Figure 6.1: Infinite array of apex-truncated pyramids placed on the interface between two half spaces (a) and definition of three-dimensional basis functions (b).

Recommendations

More research is needed to formulate the scattering problem for arbitrary polarization of the incident field and for diffraction gratings which are periodic in two dimensions. We propose a solving strategy, where we mention the main steps to realize this. The diffraction grating under consideration consist now of an infinite array of objects with a shape an apex-truncated pyramid, which is periodic in two dimensions and is placed on the interface between two half spaces, see Fig. 6.1 (a). The object will be divided into 5 tetrahedral shaped subdomains, where for each subdomain three-dimensional linear basis function may be chosen to represent the field inside the object. The three-dimensional basis functions are defined as

$$\mathbf{f}_j(\mathbf{r}) = \frac{A_j}{3V}(\mathbf{r} - \mathbf{r}_j) \tag{6.1}$$

where V is the volume of the subdomain, A_j is the surface opposite to vertex j which is positioned at $\mathbf{r}_j$ as shown in Fig. 6.1(b). At the surfaces A_j, we require that the normal component of the dielectric flux density is constant for each basis function different from zero on only one triangular surface of the tetrahedral subdomain. The electric field expressions derived in Chapter 2 and the solution strategy for periodic structures discussed in Chapter 4 can be combined to formulate the 3D scattering problem as a coupled system of integral equations. With the aid of a suitable weighting procedure, the domain integral equation results in a system of linear equations which should be solved to find the scattered electromagnetic field.

The accuracy of the diffracted field can be increased by dividing the object in a larger number of subdomains so that the field is better approximated with linear functions. This is valid for both 2D and 3D diffraction gratings.

To increase the speed of the reconstruction process, more advanced optimization methods are necessary. Therefore, sensitivity analysis should be applied to decrease the number of iteration steps [17]. Since all the formulations are written in closed form, the directional derivatives in the optimization methods can be evaluated analytically with similar accuracy.

So the proposed method seems to be a promising method to compute the scattered electromagnetic field for 2D periodic diffraction gratings with arbitrary polarization of the incident field.

Appendix A

Defined Integrals

$$I_n(s_1, s_2; d) = \int_{s_1}^{s_2} (s)^n [\ln(s^2 + d^2) - 1] ds \tag{A.1}$$

$$\begin{aligned} I_0(s_1, s_2; d) &= \int_{s_1}^{s_2} [\ln(s^2 + d^2) - 1] ds = \\ &= \left\{ s[\ln(s^2 + d^2) - 3] + 2d \arctan\left(\frac{s}{d}\right) \right\} \Big|_{s_1}^{s_2} \end{aligned} \tag{A.2}$$

$$\begin{aligned} I_2(s_1, s_2; d) &= \int_{s_1}^{s_2} s^2 [\ln(s^2 + d^2) - 1] ds = \\ &= \left\{ \frac{s^3}{3} \ln(s^2 + d^2) + \frac{2d^3}{3} \left[\arctan\left(\frac{s}{d}\right) + \frac{s}{d} - \frac{5}{6}\left(\frac{s}{d}\right)^3 \right] \right\} \Big|_{s_1}^{s_2} \end{aligned} \tag{A.3}$$

Approximation when $d \to 0$ for the integral I_n

$$\begin{aligned} \int_{s_1}^{s_2} (s)^n [\ln(s^2) - 1] ds &= \frac{1}{n+1} \int_{s_1}^{s_2} [\ln(s^2) - 1] d(s^{n+1}) \\ &= \left\{ \frac{s^{n+1}}{n+1} [\ln(s^2) - 1] \right\} \Big|_{s_1}^{s_2} - \int_{s_1}^{s_2} \frac{2s^n}{n+1} ds \\ &= \left\{ \frac{s^{n+1}}{n+1} \left[\ln(s^2) - \frac{n+3}{n+1} \right] \right\} \Big|_{s_1}^{s_2} \end{aligned} \tag{A.4}$$

Hence, when s_1 or $s_2 \to 0$ then the primitive vanish.

Appendix B

Proof Bloch's Theorem

In Section 4.3.3 we have discussed the effects of periodic media in relation to electric fields. On a physical level, when the scale of the periodicity are in the order of an electron, periodic phenomena are accurately investigated for an electron in a periodic potential. A quantum mechanical approach is essential when the scale of periodicity of the potential is in the order of the de Broglie wavelength of the electron. The mathematical formulation of a single electron in a periodic potential is governed by the Schrödinger equation which is a partial differential equation and can be solved using Bloch's theorem. In this section we will proof Bloch's theorem according to the work presented in [11]. Since, in this thesis, we investigate the electric field in periodic media, we will proof Bloch's theorem for the macroscopic case following the same procedure as for the electron in a periodic potential.

Let the Maxwell equations in the frequency domain are given by

$$\begin{aligned} \nabla \times \mathbf{H} &= \mathbf{J} - i\omega\epsilon\mathbf{E} &\quad \text{(B.1)} \\ \nabla \times \mathbf{E} &= i\omega\mu_0\mathbf{H} &\quad \text{(B.2)} \end{aligned}$$

where both the current distribution $\mathbf{J}$ and the permitivitty ϵ are periodic such that holds

$$\begin{aligned} \mathbf{J}(\mathbf{x}\text{+}\mathbf{a}) &= \mathbf{J}(\mathbf{x}) &\quad \text{(B.3)} \\ \epsilon(\mathbf{x}\text{+}\mathbf{a}) &= \epsilon(\mathbf{x}) &\quad \text{(B.4)} \end{aligned}$$

with the period indicated by $\mathbf{a}$ in a lattice with three primitive vectors $\mathbf{n}_j$, such that $\mathbf{x} = u_1\mathbf{n}_1 + u_2\mathbf{n}_2 + u_3\mathbf{n}_3$. Rewriting (B.1) in matrix form results in

$$L\begin{pmatrix} \mathbf{E} \\ \mathbf{H} \end{pmatrix} = \omega\begin{pmatrix} \mathbf{E} \\ \mathbf{H} \end{pmatrix} \quad \text{or} \quad (L - \omega\mathbf{1})\begin{pmatrix} \mathbf{E} \\ \mathbf{H} \end{pmatrix} = \mathbf{0} \tag{B.5}$$

where the operator L is defined as

$$\begin{pmatrix} 0 & \frac{i}{\epsilon}\nabla \times . - \frac{i\mathbf{J}}{\epsilon} \\ -\frac{i}{\mu_0}\nabla \times . & 0 \end{pmatrix}. \tag{B.6}$$

Since $\mathbf{J}$ and ϵ are periodic, operator L is also periodic.

Next we define a translation operator τ_a which shifts the argument of the electromagnetic field with one period, i.e.

$$\tau_a \begin{pmatrix} \mathbf{E}(\mathbf{x}) \\ \mathbf{H}(\mathbf{x}) \end{pmatrix} = \begin{pmatrix} \mathbf{E}(\mathbf{x}+\mathbf{a}) \\ \mathbf{H}(\mathbf{x}+\mathbf{a}) \end{pmatrix}. \tag{B.7}$$

The periodicity of the operator L and translation operator τ_a implies that

$$\tau_a L \begin{pmatrix} \mathbf{E} \\ \mathbf{H} \end{pmatrix} = L\tau_a \begin{pmatrix} \mathbf{E} \\ \mathbf{H} \end{pmatrix} \tag{B.8}$$

meaning that τ_a commutes with L. Two successive translations operating on the fields results in

$$\tau_a\tau_{a'} \begin{pmatrix} \mathbf{E}(\mathbf{x}) \\ \mathbf{H}(\mathbf{x}) \end{pmatrix} = \tau_a \begin{pmatrix} \mathbf{E}(\mathbf{x}+\mathbf{a}') \\ \mathbf{H}(\mathbf{x}+\mathbf{a}') \end{pmatrix} = \begin{pmatrix} \mathbf{E}(\mathbf{x}+\mathbf{a}'+\mathbf{a}) \\ \mathbf{H}(\mathbf{x}+\mathbf{a}'+\mathbf{a}) \end{pmatrix} = \tau_{a'+a} \tag{B.9}$$

showing that the translation operator commutes. Since the two operators from a set of commuting operator, the eigenvectors of Eq. (B.5) and the eigenvectors of operator τ_a lie in the same space. This implies that we may express the electromagnetic field as the solution of eigenvectors of τ_a, i.e.

$$[\tau_a - c(\mathbf{a})] \begin{pmatrix} \mathbf{E} \\ \mathbf{H} \end{pmatrix} = 0 \tag{B.10}$$

where the eigenvectors, $c(a)$, are related to the translation operator by

$$\tau_a\tau_{a'} \begin{pmatrix} \mathbf{E} \\ \mathbf{H} \end{pmatrix} = c(a)\tau_{a'} \begin{pmatrix} \mathbf{E} \\ \mathbf{H} \end{pmatrix} = c(\mathbf{a})c(\mathbf{a}') \begin{pmatrix} \mathbf{E} \\ \mathbf{H} \end{pmatrix} \tag{B.11}$$

where we used Eq. (B.9). From calculus we known that the solution of partial differential equations are harmonic functions so that we assume that the solution of (B.10) can be written in the following form

$$c(\mathbf{n}_j) = \exp(ik_j) \qquad \text{for} \qquad j = \{1,2,3\} \tag{B.12}$$

for an appropriate choice of k_j. As a consequence of (B.9), the substitution of $\mathbf{x}$ in Eq. (B.12) leads to

$$c(\mathbf{x}) = c(\mathbf{n}_1)^{u_1} c(\mathbf{n}_2)^{u_2} c(\mathbf{n}_3)^{u_3}. \tag{B.13}$$

When we define a vector composed of reciprocal lattice vectors, $\mathbf{b}_i$, which satisfies the condition that $\mathbf{b}_i \cdot \mathbf{n}_j = \delta_{ij}$, we rewrite (B.13) as

$$c(\mathbf{x}) = \exp(i\mathbf{k} \cdot \mathbf{x}) \tag{B.14}$$

where

$$\mathbf{k} = k_1\mathbf{b}_1 + k_2\mathbf{b}_2 + k_3\mathbf{b}_3. \tag{B.15}$$

Hence, from Eq. (B.7), (B.10) and (B.14) we find the Bloch condition, i.e.

$$\begin{pmatrix} \mathbf{E}(\mathbf{x}+\mathbf{a}) \\ \mathbf{H}(\mathbf{x}+\mathbf{a}) \end{pmatrix} = \exp(i\mathbf{k} \cdot \mathbf{a}) \begin{pmatrix} \mathbf{E}(\mathbf{x}) \\ \mathbf{H}(\mathbf{x}) \end{pmatrix}. \tag{B.16}$$

In conclusion, we have proven that the solutions of the electromagnetic equations for a periodic medium can be expressed in terms of Bloch waves which satisfies the Bloch condition (B.16). By including only one primitive vector in $\mathbf{x}$ and $\mathbf{k}$ we easily find the expression, as used in Chapter 4, where periodicity is along one spatial coordinate.

Bibliography

[1] P.M van den Berg, "Rigorous diffraction theory of optical reflection and transmission gratings", Ph.D. Thesis, Delft University of Technology, 1971.

[2] N.P. van der Aa, "Sensitivity analysis for grating reconstruction", Ph.D. Thesis, University of Technology Eindhoven, 2007.

[3] R. Petit, et al., "Electromagnetic theory of gratings", Springer, Berlin, 1980.

[4] M.C. van Beurden, "Integro-differential equations for electromagnetic scattering: analysis and computation for objects with electric contrast", Ph.D. Thesis, University of Technology Eindhoven, 2003.

[5] A.P.M. Zwamborn, "Scattering by object with electric contrast", Ph.D. Thesis, University of Technology Delft, 1991.

[6] R.M. Shubair and Y. L. Chow, "Efficient Computation of the Periodic Green's Function in Layered Dielectric Media", IEEE Transaction on Microwave Theory and Techniques, Vol. 41. No. 3, 1993.

[7] B.J. Morsink, "Fast Modeling of Electromagnetic Fields for the Design of Phased Array Antennas in Radar Systems", Ph.D. Thesis, University of Technology Eindhoven, 2005.

[8] E.J. Rothwell and M.J. Cloud, "Electromagnetics," CRC Press, 2001.

[9] M. Abramowitz and I. A. Stegun, "Handbook of Mathematical Functions with Formulas, Graphs, and Mathematical Tables", Dover, New York, 1964.

[10] A.G. Tijhuis, "Plane-wave Excitation of Two-Dimensionally Periodic Metallized Structures in Plane-Stratified Dielectric Media", Report of Study Contract WDC262A "Frequency Selective Surfaces" between Thales Naval Nederland and the faculties of Electrical Engineering and Mathematics and Computer Science of the Eindhoven of Technology, Eindhoven, 2002.

[11] N.W. Ashcroft and N.D. Mermin , "Solid state physics", Saunders College Publ., London, 1976.

[12] E. Kreyszig, "Introductory functional analysis with applications", Reprint, Wiley, New York, 1989.

[13] Z.Q. Peng and A.G. Tijhuis, "Transient Scattering by a Lossy Dielectric Cylinder: Marching-on-in-Frequency Approach", Journal of Electromagnetic Waves and Applications, Vol. 7, No. 5, 739-763, 1993.

[14] S. M. Rao, D. R. Wilton, and A. W. Glisson, "Electromagnetic scattering by surfaces of arbitrary shape," IEEE Trans. Antennas Propagat., vol. 30, pp. 409-418, May 1982.

[15] R.F. Harrington, "Field Computation by Moment Methods", Macmillan, London, 1968.

[16] M. Nevière, E. Popov, "Light Propagation in Periodic Media: Differential Theory and Design", CRC Press, 2002.

[17] P. van Leuven, "Shape Sensitivities of Perfectly Conducting 2D Objects and Inverse Scattering", M.Sc. Thesis, 2007.

Summary

The developments in electromagnetic modeling of inverse scattering problems has become an important topic for analysis of periodic structures called diffraction gratings. An application where diffraction gratings are used is in novel lithography machinery. In this applications diffraction gratings are placed on a wafer (a round substrate) for positioning purposes. To obtain position information and in general information about shape of the grating, the structure is illuminated by a monochromatic electromagnetic plane wave. The result is a discrete set of diffracted waves radiating in different directions which are prescribed by the angle of incidence of the incident field, the wavelength and the period of the grating.

In numerical models, the scattered electromagnetic far-field is computed for a diffraction grating with an arbitrary chosen geometry after which the computed field can be compared with the measured field. The measured field contains information with respect to the shape of the grating which is a priori not known. Then by varying the geometrical parameters in the numerical model, the difference between the measured field and the computed field can be minimized in a number of iterations. The geometrical parameters corresponding to the lowest difference give the best reconstruction of the actual grating. The reconstruction strategy is quite time consuming since the electromagnetic field should be computed for a large number of different geometrical parameters in the numerical scattering model. In lithography applications, the requirement is that the shape of the grating should be fastly retrieved and with an accuracy in the order of nanometers.

Therefore, in this thesis, we propose a fast and efficient solution strategy to compute the scattered electric field for an object periodic in one direction placed on the interface between two half spaces with different electromagnetic properties. We have considered only the case where the diffraction grating is illuminated by a plane wave electrically polarized in the invariant direction of the grating. The scattering problem for the electric field is therefore formulated in the form of a domain integral equation valid in a two dimensional domain. The periodicity is expressed in the electric field by using a Floquet modal expansion. The Floquet modal coefficients, or reflection coefficients, are written in terms of spatial Fourier transforms where a spectral and spatial domain approach is used to accomplish this. The evaluation of the spatial Fourier transform in the scattering problem is restricted to only one single period of the grating. The general idea to solve this scattering problem is based on the assumption that the wavelength of the electric field inside the object is large compared to the maximum dimension of the object. The electric field can therefore be approximated by linear functions. To solve the integral equation for the electric

field, we have used the point matching method, as special case of the method moments where linear functions as basis functions and Dirac delta functions as test functions are used. The integral equation reduces to a relative small system of equations where furthermore all formulations are expressed in a closed form.

As a feasibility study, we have first considered the case of a non-periodic infinitely long dielectric cylindrical object with trapezoidal object is placed in free space. The developed method was compared with an alternative solution method. Numerical computations have shown that the diffracted electric far-field is found with a relative error in the order of 0.2% when the wavelength of the electric field in free space λ_0 is at least ten times larger than the maximum dimension (L_{max}) of the object ($\lambda_0 > 10L_{\text{max}}$) for objects with relative low electric contrast. The trapezoidal object is discretized in two triangular subdomains where at each subdomain three linear basis functions are used to approximate the electric field.

For diffraction gratings, the diffraction efficiencies are found with an error in the order of 0.1%. The corresponding geometrical parameters (the top width and the height and a priori known bottom width) of a diffraction grating consisting of a array of cylindrical objects with a trapezoidal cross section placed on the interface between two half spaces are reconstructed with a relative error in the range of 1-6%. We have observed that the height is more sensitive to variations in the reconstruction process such that height should be optimized first after which the width can be found.

The fact that the scattering problem is formulated in a closed form means that the electric field can be computed very fast. It allows thus a quick reconstruction of the shape of the diffraction grating, but with limited accuracy. This method delivers a quite good rough estimate of the geometry of the grating which is extremely suitable for an first guess of the shape of the grating in more accurate but slower solution methods.

Further, the proposed solution strategy can be easily extended to three-dimensional diffraction gratings illuminated by an arbitrary polarization of the incident field. For the three-dimensional case, the accuracy of the reconstruction process and computational effort will be comparable with the methods derived and discussed in this thesis. Since the scattering problem is formulated in a closed form, the application of the sensitivity analysis on the electromagnetic field formulation can be done analytically, which will increase the speed of the iterative reconstruction process.

So, for diffraction gratings periodic in one direction, the solution strategy has proven to be fast and efficient in reconstructing the geometrical parameters of the grating. The general set-up of the formulation of the scattering problem enables the possibility to express the electromagnetic field for other shaped diffraction gratings and polarization of the incident field.

Acknowledgements

At the end of this Master of Science project I would like to thank a number of people who where very helpful to me. The first person I would like to thank is prof. Anton Tijhuis for offering me the opportunity to work in this challenging project. The many valuable conversations and discussions on the field of electromagnetics and other interesting topics helped me to complete the work.

Second I would like to thank dr. Emilia Motoasca my "daily" supervisor. I will think back to the many stimulating and valuable discussions and how she guided me through the difficult provisional patent application process.

Further, I would like to thank dr. Irwan Setija from ASML for the hospitality and the interesting discussions at the beginning and end of this graduation project.

And last but not least I would like to thank the members of the electromagnetics group of Eindhoven. In particular I would to thank dr. Martijn van Beurden for his help.

Michiel Sprée
February 2009